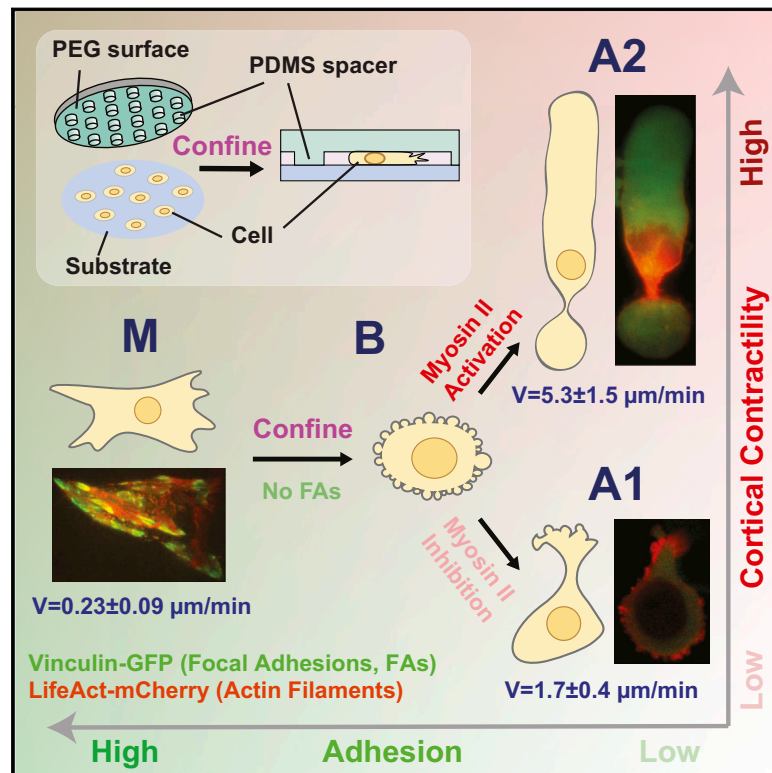


Confinement and Low Adhesion Induce Fast Amoeboid Migration of Slow Mesenchymal Cells

Graphical Abstract



Authors

Yan-Jun Liu, Maël Le Berre, ..., Raphaël Voituriez, Matthieu Piel

Correspondence

mael.leberre@curie.fr (M.L.B.),
matthieu.piel@curie.fr (M.P.)

In Brief

A large range of slow mesenchymal cells can switch to fast amoeboid-like migration under conditions of low adhesion and strong confinement, suggesting that tumor cells may spontaneously escape primary tumors and invade tissues without any specific genetic alteration.

Highlights

- Physical confinement and low adhesion induce the mesenchymal-amoeboid transition
- A large range of slow mesenchymal cell types can display fast amoeboid-like migration
- A fast mode (A1) and a faster and more conserved contractile mode (A2) were observed
- A2 migration could be an ancestral migratory behavior shared among eukaryotes



Confinement and Low Adhesion Induce Fast Amoeboid Migration of Slow Mesenchymal Cells

Yan-Jun Liu,^{1,6} Maël Le Berre,^{1,6,*} Franziska Lautenschlaeger,^{1,3} Paolo Maiuri,¹ Andrew Callan-Jones,⁵ Mélina Heuzé,¹ Tohru Takaki,⁴ Raphaël Voituriez,² and Matthieu Piel^{1,*}

¹Institut Curie, CNRS UMR 144, 26 rue d'Ulm, 75005 Paris, France

²Laboratoire Jean Perrin and Laboratoire de Physique Théorique de la Matière Condensée, CNRS/Université Pierre et Marie Curie, 75005 Paris, France

³Universität des Saarlandes, Campus E2 6, 3. OG, Zi. 3.17, 66123 Saarbrücken, Germany

⁴Cancer Research UK London Research Institute, Clare Hall Laboratories, Blanche Lane, South Mimms, Hertfordshire EN6 3LD, UK

⁵Laboratoire Matière et Systèmes Complexes, CNRS/Université Paris Diderot, UMR 7057, 75204 Paris Cedex, France

⁶Co-first author

*Correspondence: mael.leberre@curie.fr (M.L.B.), matthieu.piel@curie.fr (M.P.)

<http://dx.doi.org/10.1016/j.cell.2015.01.007>

SUMMARY

The mesenchymal-amoeboid transition (MAT) was proposed as a mechanism for cancer cells to adapt their migration mode to their environment. While the molecular pathways involved in this transition are well documented, the role of the microenvironment in the MAT is still poorly understood. Here, we investigated how confinement and adhesion affect this transition. We report that, in the absence of focal adhesions and under conditions of confinement, mesenchymal cells can spontaneously switch to a fast amoeboid migration phenotype. We identified two main types of fast migration—one involving a local protrusion and a second involving a myosin-II-dependent mechanical instability of the cell cortex that leads to a global cortical flow. Interestingly, transformed cells are more prone to adopt this fast migration mode. Finally, we propose a generic model that explains migration transitions and predicts a phase diagram of migration phenotypes based on three main control parameters: confinement, adhesion, and contractility.

INTRODUCTION

The mechanisms individual cells use to migrate can be divided into two distinct types, known as mesenchymal migration and amoeboid migration. Cells migrating in a mesenchymal fashion typically adopt an elongated, spindle-like shape and exert traction on their substrates via focal adhesions associated with actin rich protrusions, such as lamellipodia or filopodia. In contrast, cells undergoing amoeboid migration adopt round or irregular shapes. They undergo cycles of expansion and contraction, which allow them to squeeze through gaps in the extracellular matrix. The velocity of amoeboid migration is often higher than that of mesenchymal migration (Panková et al., 2010) and it appears to involve a range of different sub-modes, such as bleb-based migration or gliding (Paluch and Raz, 2013). Consequently, it is not as

well-defined at the molecular level as mesenchymal migration, although it is thought to rely on an increased activity of the RhoA pathway, which activates formin-based actin nucleation and myosin II contractility (Sanz-Moreno and Marshall, 2010).

Despite an extensive literature on the subject, it remains unclear whether the various modes of amoeboid migration are mechanistically distinct from each other, or whether they represent a continuum of a single process. Recent work, however, has identified mechanisms common to several forms of amoeboid migration, supporting the continuum model. Several studies report, for example, that amoeboid migration is often based on a contractile cell rear inducing a retrograde flow in the cell cortex (Heuzé et al., 2013; Paluch and Raz, 2013; Poincloux et al., 2011). Others have shown that, in contrast with mesenchymal migration, amoeboid migration does not depend on a cell's ability to form focal adhesions with its environment (Bergert et al., 2012; Lämmermann et al., 2008; Renkawitz et al., 2009). In the light of these studies, Lämmermann and Sixt (2009) have proposed that three key parameters modulate the mode of migration of cells, namely protrusion, contractility, and adhesion. They further suggest that by altering the balance between these parameters, cells could adapt their mode of motility to different migration environments (Lämmermann and Sixt, 2009), allowing migrating cells to negotiate the topologies of the different tissues they encounter.

Migration mode plasticity is an important factor for immune cells migration but also in cancer metastasis, as disseminating tumor cells have to navigate a range of extracellular matrix geometries to escape their point of origin and spread to distant sites. Metastasizing cancer cells exhibit both mesenchymal and amoeboid modes of migration, and recent studies have shown that they can switch between the two, a phenomenon known as the mesenchymal-amoeboid transition (MAT) (Friedl and Wolf, 2003; Panková et al., 2010; Taddei et al., 2013; Tozluoğlu et al., 2013). Importantly, non-migrating cells such as epithelial cells can first undergo a transition to mesenchymal migration (epithelial to mesenchymal transition or EMT), enabling them to develop collective and/or individual migratory behaviors associated with cancer cell dissemination (Friedl and Wolf, 2003; Taddei et al., 2013). This suggests that, by going through sequential transitions, even epithelial cells, could eventually display amoeboid motility (Giampieri et al., 2009).

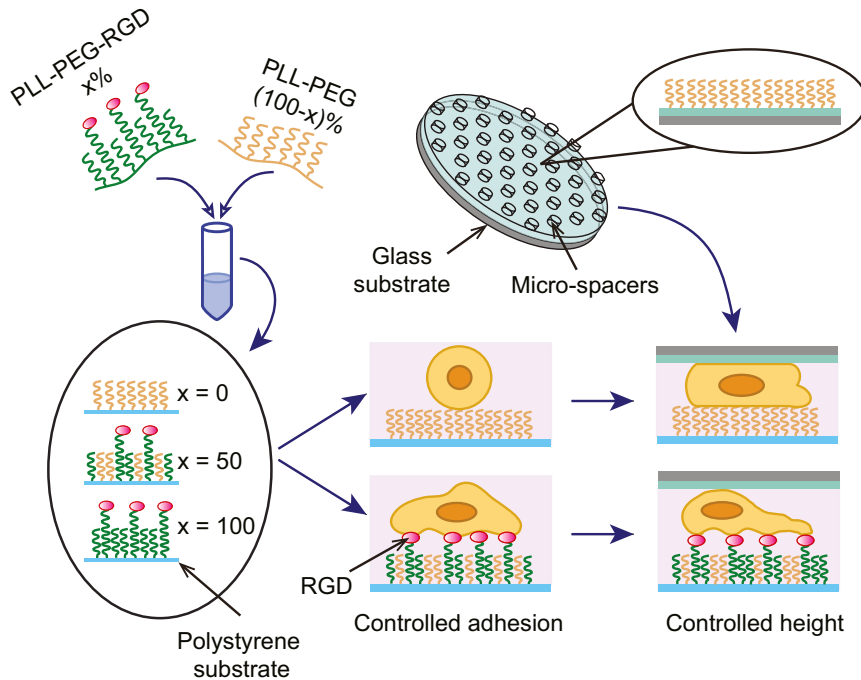


Figure 1. Schematic Diagram of Cell Migration Assay

Cell culture substrates were treated with various ratios of pLL-PEG and pLL-PEG-RGD to control adhesion of cells with their environment and PEG-treated slides containing micro-spacers were used to confine cells at a fixed height. See also [Figure S1](#).

density of RGD peptides on the cell substrate) ([Barnhart et al., 2011](#)) and to confine cells plated on a 2D substrate ([Figure S1](#); [Le Berre et al., 2012](#)).

Normal human dermal fibroblast cells (NHDF) migrate in a mesenchymal fashion and so were chosen to study. We began by seeding NHDF cells on surfaces coated with various concentrations of pLL-PEG-RGD, but without confining them ([Figure 2A](#)). As RGD density decreased, cell spreading likewise decreased. Where RGD density dipped below 5%, cells were unable to attach to the substrate when gently flushed ([Figures 2B and 2C](#)).

To quantify differences in migration behavior, trajectories of individual cells ([Figure 2D](#)) were analyzed in terms of instantaneous speed (S), persistence (P) and diffusivity (D) ([Figures 2E, S2D, and S2E](#); [Movie S1](#); see [Extended Experimental Procedures](#) for details on calculation). In agreement with previous work by others ([DiMilla et al., 1993](#)), the long-term displacement of cells, which is characterized by their diffusion coefficient, is maximal for an intermediate level of adhesion ([Figure 2F](#)), due to an increase in persistence and a decrease in instantaneous speed with increasing adhesion ([Figures 2G and 2H](#)). These observations confirmed the typical mesenchymal migration of these fibroblasts.

Confinement Modifies the Migration Behavior of NHDF Cells

We introduced confinement by covering cells (cultured on surfaces of controlled adhesion) with a non-adhesive surface ([Figure S1](#)). NHDF cells were $7.6 \pm 0.36 \mu\text{m}$ high during interphase. We therefore chose to limit our investigation to heights of either 5 or 3 μm . At 5 μm (low confinement), the cell body was slightly deformed. At 3 μm (high confinement), both the cell body and the nucleus were deformed ([Le Berre et al., 2012](#)).

Cells tended to retract when confined, forming fewer large lamellipodial protrusions and more elongated pseudopodia ([Movie S2](#); [Figure 3A](#) for 5 μm , [Figure S3A](#) for 3 μm , and phenotype C in [Figures 3B–3E](#)). This retraction of the cell margin was probably due to an increase in cell cortex contractility, which favors a more compact morphology ([Sahai and Marshall, 2003](#)). When adhesion was low ($\leq 15\%$ RGD) and confinement high, cells became totally round, mostly immobile, and often showed a continuous blebbing activity ([Movie S2](#); phenotype B in [Figures](#)

Given its importance in metastasis, the MAT has been the focus of several recent studies. These have identified key parameters driving the transition: cell-intrinsic factors, such as intracellular signaling and contractility, and extrinsic, environmental factors, such as cell adhesion and the geometry of the extracellular matrix. Using a protease inhibitor mix to inhibit the matrix remodeling ability of mesenchymal cells induces the MAT and is associated with a reduction in integrin expression ([Carragher et al., 2006](#); [Wolf et al., 2003](#)). [Tozluoglu et al. \(2013\)](#) combined in vivo experiments and mathematical simulations to highlight cell confinement as a crucial parameter affecting the efficiency of various migration modes. In vitro studies using micro-channels also point to an important contribution of confinement in changing the requirements for efficient locomotion ([Hung et al., 2013](#)).

Until now, however, no systematic quantitative study has been performed to understand the interplay between a cell's environment and its migration behavior. Here, we describe how we systematically studied the effects of confinement and adhesion on migration modes. Using a variety of cell types, we found that slow mesenchymal cells can switch to fast amoeboid-like migration under conditions of low adhesion and high confinement. We propose a simple generic physical model that produces a phase diagram of migration modes and depends on both the intrinsic properties of cells and environmental parameters.

RESULTS

Adhesion Decreases Speed but Increases Persistence in Non-Confined Conditions

To systematically investigate the effects of adhesion and confinement on cell migration, we combined two methods ([Figure 1](#)) to control cell adhesion (by quantitative controlling of the

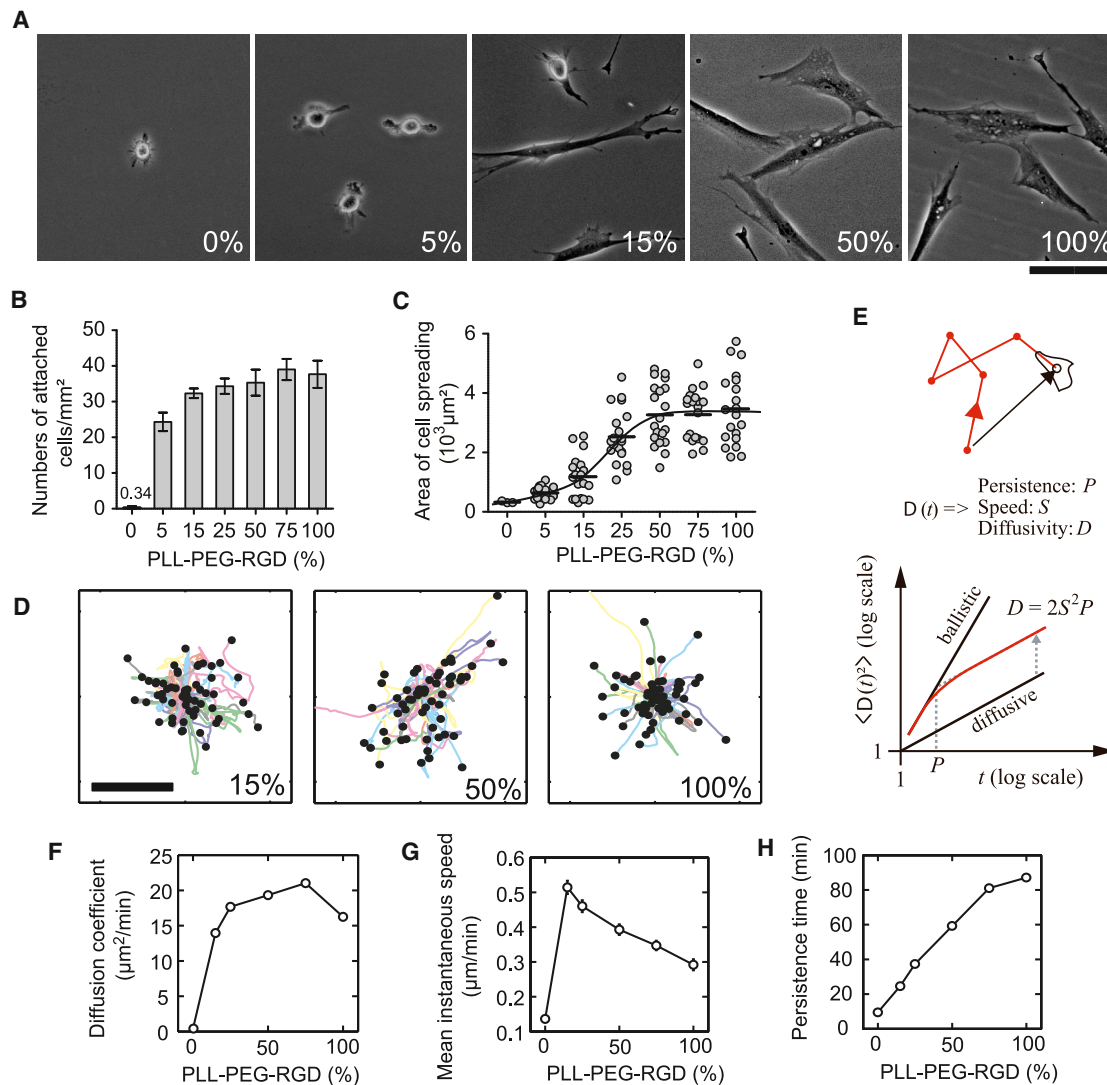


Figure 2. Migration Behavior of NHDF Cells on Surfaces of Various Adhesive Levels

(A) Representative phase contrast images of NHDF cells on surfaces containing various RGD densities.

(B and C) Quantification of the number of attached cells per mm² (B) and their spreading areas (C) for various RGD densities ($n \geq 20$ cells, $N \geq 2$ experiments for each point on the graph).

(D) Representative trajectories of 60 cells recorded over 24 hr for various RGD densities. The starting positions of each cell were registered to the center of the plot.

(E) Schematic explaining measurements of cell displacement $D(t)$, mean instantaneous speed (S), and persistence (P) of cells (see [Supplemental Information](#)).

(F–H) Graphs showing diffusion coefficient (F), mean instantaneous speed (G), and persistence time (H) of NHDF cells for various RGD densities ($n > 100$ cells for each point on the graph). In (A)–(H), % corresponds to the percentage of pLL-PEG-RGD in both pLL-PEG and pLL-PEG-RGD solution, error bars indicate SEM, and scale bars represent 100 μm .

See also [Figure S2](#) and [Movie S1](#).

3B–3E, note in [Figure S3](#) legend), further suggesting an increased level of contractility. Unexpectedly, a fraction of these rounded NHDF cells could polarize and move fast with an amoeboid-like morphology ([Movie S2](#); phenotype A in [Figures 3B–3E](#)).

Further quantification of the migration of spread cells (phenotype C or E) showed that confinement always reduced the instantaneous speed of such cells ([Figure 3E](#)), but did not significantly change their persistence ([Figure S3B](#)). Cells that were more rounded did not move, except for a sub-fraction of cells that spontaneously polarized (phenotype A). These cells showed

a much higher diffusion coefficient (up to ten times higher), which was not observed under conditions of strong adhesion or without confinement. The high diffusion coefficient of cells showing an amoeboid-like behavior could be attributed to both an increase in instantaneous speed and an increase in persistence. This is reminiscent of the behavior of leukocytes, such as dendritic cells, which are known to migrate fast and independently of specific integrin-based adhesion ([Lämmermann et al., 2008](#); [Lämmermann and Sixt, 2009](#); [Hawkins et al., 2009](#); [Heuzé et al., 2013](#)).

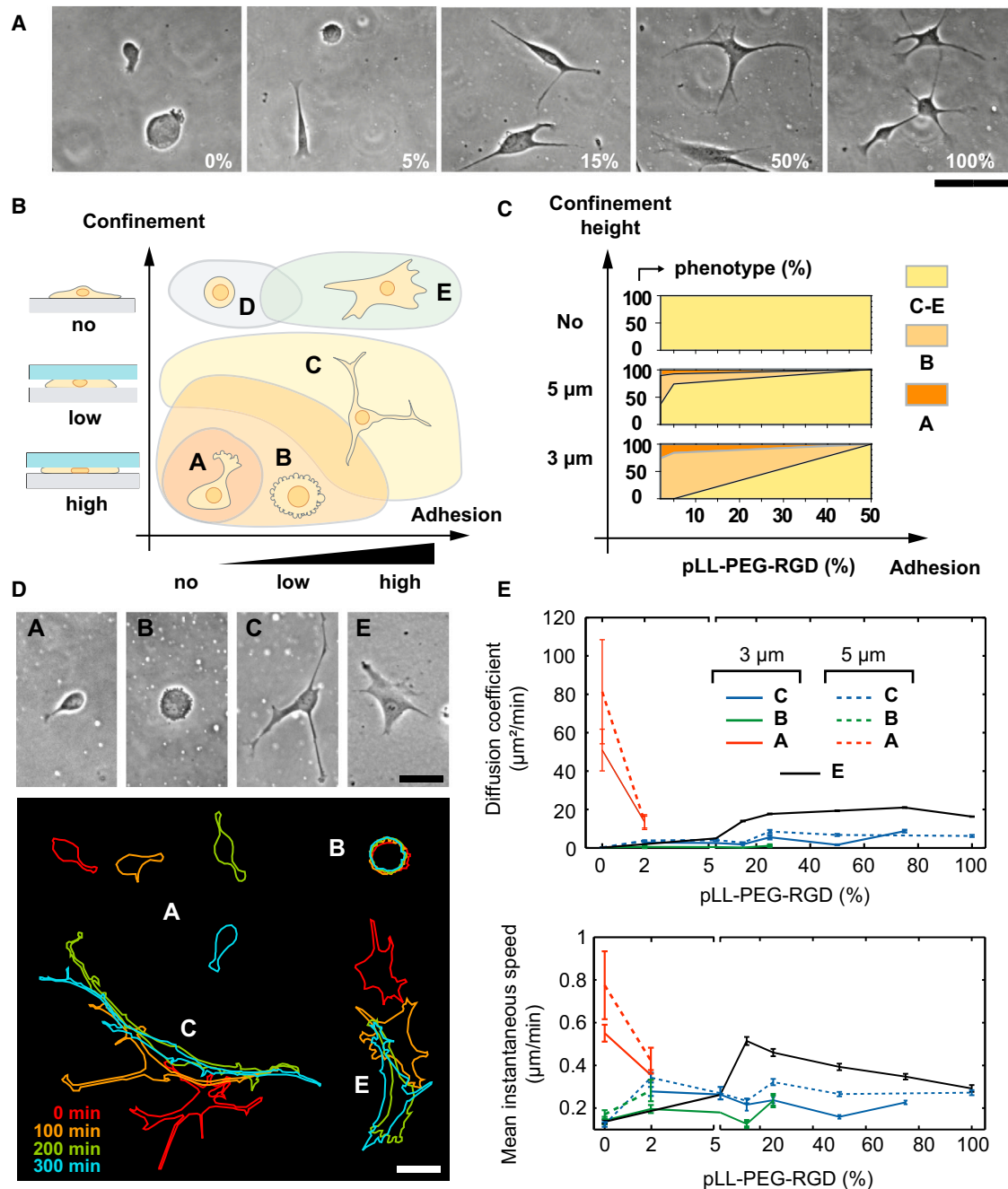


Figure 3. Migration Behavior of NHDF Cells in Response to Varying Confinement Height and Adhesion Strength

(A) Representative phase contrast images of NHDF cells under 5 μm confinement and various RGD densities. Scale bar represents 100 μm .
 (B) Schematic showing the appearance of the observed phenotypes as a function of confinement height and adhesion strength. Phenotypes are defined as follows: A, round cell with a leading edge; B, round cell; C, cell with long and non-spread pseudopodia; D, floating, round cell; E, normally spread cell.
 (C) Portion of the different phenotypes observed under various conditions according to cell morphologies defined in (B). $n \geq 100$ cells for each conditions.
 (D) Top panel: representative images of cells for each phenotype. Conditions of confinement (μm)/adhesion (% pLL-PEG-RGD) are A: 5/2%; B: 3/15%; C: 3/75%; E: no/100%. Bottom panel: corresponding time lapse of the cell outline. The color of the outlines represents elapsed time after the first outline. Scale bar represents 50 μm .
 (E) Graph showing diffusion coefficient (top) and instantaneous speed (bottom) of each NHDF phenotype on varying RGD densities and for different confinements. Error bars indicate SEM.

See also [Figure S3](#) and [Movie S2](#).

Altogether, these observations show that a fraction of typically mesenchymal NHDF cells migrating under conditions of high confinement and low adhesion can switch to a fast amoeboid-like migration.

Two Distinct Modes of Amoeboid-like Migration Can Be Induced, Depending on Cell Type

To test whether this microenvironment-dependent switch in the mode of migration was restricted to NHDF cells, we investigated the migration behavior of 20 other cell types confined by fully non-adhesive surfaces (100% pLL-PEG). We chose a sample of cell types covering a large range of migratory and non-migratory cells, including normal and transformed epithelial cells (pre- and post-EMT), normal and transformed mesenchymal cells, leukocytes (typical amoeboid cells), and muscle cell precursors.

For all cell types, with the exception of normal epithelial cells, we found a sub-fraction of spontaneously polarizing cells moving fast with an amoeboid-like morphology (Figures 4A and 4B). Unexpectedly, we found two distinct types of fast-migrating cells (Figures 4A and S4A–S4C). The first type, which we named A1, was similar to what was observed with NHDF cells: a round cell body and a small leading edge (Movie S3). The second, which we named A2, had an elongated ellipsoid cell body with a large uropod and resembled a migrating neutrophil (Figures S4A and S4B; Movie S3). Globally, A2 cells moved significantly faster ($5.3 \pm 1.5 \mu\text{m}/\text{min}$) than A1 cells ($1.7 \pm 0.4 \mu\text{m}/\text{min}$) and they both moved much faster than mesenchymal controls ($0.234 \pm 0.09 \mu\text{m}/\text{min}$) (see Figures 4C and 4D).

The type of fast migration, A1 or A2, varied according to the cell line under observation (Figure 4D). For five cell types, the two modes could coexist in the same cell population, while most cell types preferentially switched to one migration mode or the other. Interestingly, different sub-clones of HeLa cells obtained from different labs (see Supplemental Information for a description of cell types) could either preferentially switch to A1 or A2 (Figure 4D). This suggests that these two migration modes, which are morphologically very different, can arise in very similar cell types, probably based on subtle molecular differences.

Transformed Cells, as well as Leukocytes, Preferentially Display Fast A2 Migration under Confinement

Comparing different groups of cell types revealed general trends in the transition to amoeboid migration. Normal epithelial cells rarely displayed a transition to fast amoeboid migration (Figure 4D). This was due to the formation of large cell clusters that were mostly non-motile. At lower density, individual cells were able to display the A1 migratory phenotype.

When we induced EMT in MDCK or MCF10A cells with TGF β , they no longer formed clusters and displayed fast A2 migratory phenotype. This was also true for tumor cell lines of epithelial origin from different tissues or in vitro transformed cell lines. Similarly, while normal mesenchymal cells tended to display mostly A1 migration under confinement, transformed mesenchymal cells often used in MAT studies displayed a high proportion of A2 migration mode when confined in a non-adhesive environment. Surprisingly, even muscle cell precursors displayed this fast migratory behavior under strong confinement. As expected, all leukocytes displayed A2-like migration,

including monocytes, which showed no motility on 2D substrates due to lack of adhesion. This suggested that the fast A2 migration mode was typically adopted by amoeboid cells, such as leukocytes, and by transformed cells migrating individually, independently of their tissue of origin.

Altogether, these results show that most slow mesenchymal cells can spontaneously switch to a fast amoeboid-like mode of migration when they are confined in a non-adhesive environment.

The Switch to Amoeboid-like Migration Depends on the Absence of Focal Adhesions

The switch to amoeboid migration was observed only for adhesion levels that did not allow cell binding to the substrate when no confinement was applied (Figures 2B and 3C). To check for the presence of focal adhesions, we imaged HeLa VL cells by total internal reflection microscopy (TIRFM) (Trache and Meininger, 2008), on fibronectin-coated substrates and on PEG-treated substrates. On fibronectin, Vinculin-GFP displayed the expected pattern of focal adhesions, while on PEG, it was diffuse in the cytoplasm (Figure S5A). This was true both with and without confinement, showing that confinement did not restore the capacity of cells to form focal adhesions on PEG-treated surfaces.

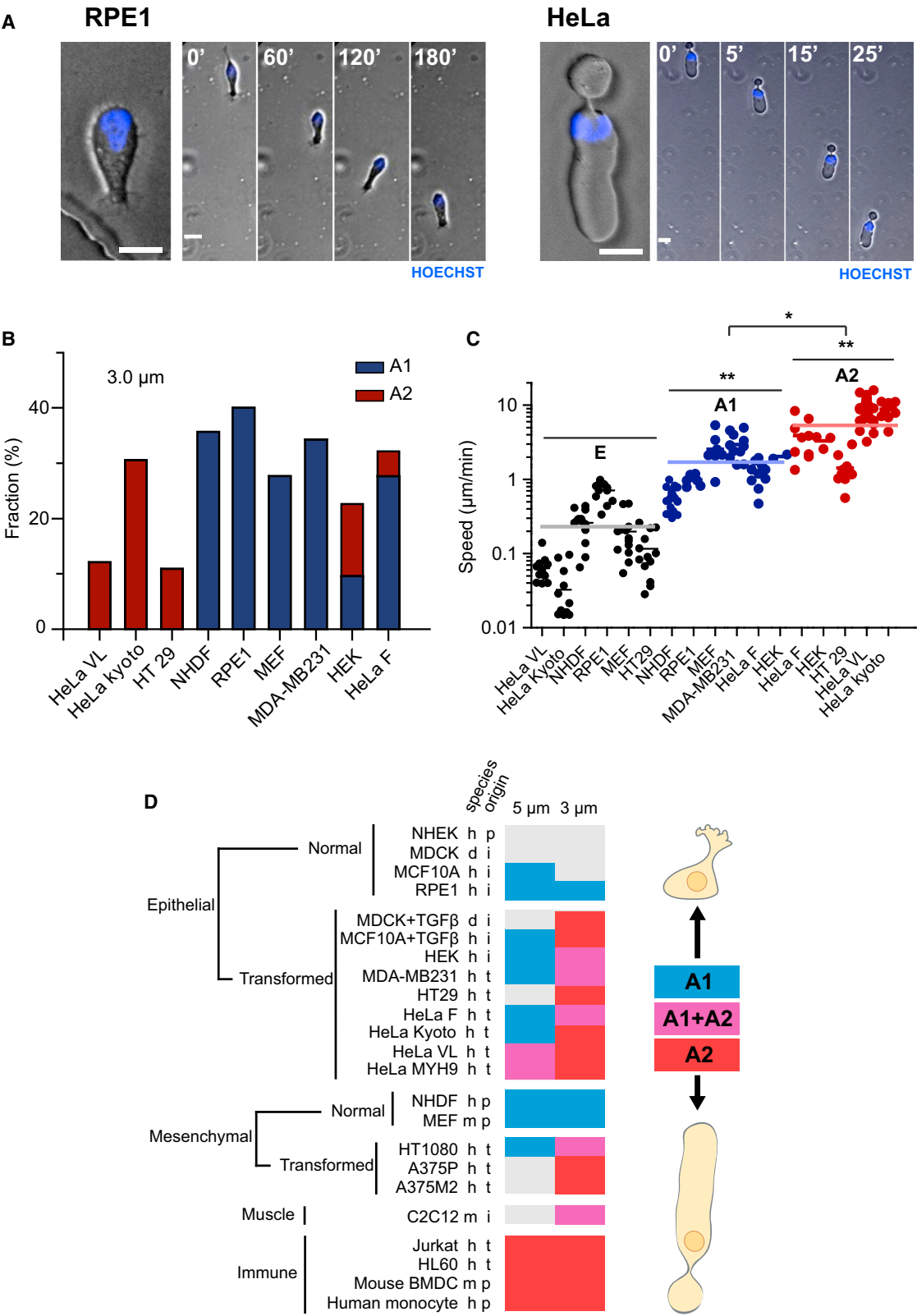
We then tested whether the ability of PEG-treated substrates to promote amoeboid migration relied on a lack of focal adhesions or on another surface effect of the PEG treatment. For this, we confined HeLa VL on an adhesive fibronectin surface and prevented formation of focal adhesions by knocking down the expression of Talin proteins with small interfering RNA (siRNA) or using the β 1-integrin-blocking antibody 4B4 (Figures 5, S5B, and S5F).

Under confinement on a fibronectin-coated surface, Talin knocked-down cells switched to A2 three times more often than cells treated with a non-targeting siRNA and as often as control cells on a non-adhesive PEG-treated substrate. Similarly, treating cells with 4B4 significantly increased the proportion of cells switching to amoeboid migration. This confirmed that the capacity to switch to amoeboid-like migration depended on the absence of focal adhesions and not on the chemical nature of the migration substrate or on a particular molecular perturbation of focal adhesion complexes.

The Switch to Fast A2 Amoeboid-like Migration Depends on High Cell Contractility, whereas A1 Requires Low Contractility

The comparison of a large number of cell types under two different levels of confinement suggested that increasing confinement led to a larger proportion of A2 migrating cells (Figure 4D). We confirmed this effect using three different levels of confinement for HeLa VL cells. While most migrating cells displayed A1 migration under low confinement, only A2 was observed under high confinement (Figure 5B).

To investigate the role of the myosin II motor protein in the behavior of confined cells, we first treated confined HeLa VL cells with increasing doses of the phosphatase inhibitor calyculin A. This inhibits the dephosphorylation of myosin II, thereby increasing its activity (Ishihara et al., 1989). Increasing calyculin A concentration increased the fraction of cells switching to A2



(legend on next page)

migration mode, up to 66% of the total population (Figures 5C and 5D; Movie S4). We also used siRNA to knock down the expression of MYPT1 (Figure S5F), the PP1 partner targeting myosin II (Feng et al., 1999). MYPT1 siRNA induced an increase in the volume and number of blebs (Figure S5C) and an increase in the fraction of cells switching to A2 (Figures 5E and S5D), confirming the role of myosin II-based contractility in this phenomenon.

High-resolution imaging showed that the transition to A2 corresponded to the formation of a large bleb where most of the cell cytoplasm, including the nucleus, was transferred (Figure 5F; Movie S5), inducing a profound reorganization of the cytoskeleton and resulting in a new stable shape with an elliptical cell body and a rear uropod. The formation of such large blebs occurred at a constant rate (Figure S5E) and more frequently when cells were treated with calyculin A or knocked-down for MYPT1 (Figure S5E). Overall, this suggests that confinement favors cell contractility and that high cell contractility favors fast A2 migration.

To confirm that hypothesis, we measured the contractility of cell populations displaying different fractions of A2 phenotype (see Supplemental Information). We plated cells between two non-adhesive gels of known rigidity (1 kPa) coated with fluorescent beads (Figure S5H). Using 3D high-resolution imaging, we assessed the extent to which the cells deformed the gels and so deduced the ability of cells to push on their surroundings, as a measure of their relative level of cortical contractility (Figure S5I). This measure increased with increasing myosin II activity (Figures 5H and S5G), and stronger cells displayed a higher fraction of A2 migratory phenotype (Figure 5H). We then assayed other cell types and found that cells displaying A2 migration were significantly stronger than cells displaying A1 migration (Figure 5I). This confirmed our hypothesis that A2 migration appeared above a certain threshold of contractility.

Accordingly, treating cells with the ROCK inhibitor Y27632 reduced bleb formation and the proportion of cells switching to A2. More generally treatment with blebbistatin prevented formation of A2 migrating cells in all cell types tested. Unexpectedly, however, it did not prevent HeLa cells from moving and instead drastically increased the number of cells switching to the A1 amoeboid-like migration mode (Figures 5C and 5G; Movie S4).

Together, these experiments show that high contractility favored fast A2 migration mode, by increasing blebbing activity, eventually leading to the formation of large “stable blebs” comprising most of the cell content. Conversely, low contractility favored the formation of protrusive structures, leading to A1 migration.

A2 Migration Mode Relies on a Fast and Global Cortical Retrograde Flow, whereas A1 Migration Relies on Local Actin Polymerization

To characterize the migration mechanism of confined non-adhesive cells, we imaged focal adhesions, actin, and myosin II using TIRFM. On the fibronectin-coated surface, cells attached, spread, and formed focal adhesions and actin stress fibers containing myosin II (Figure 6A, upper panel; Movie S6). In A2 cells migrating under confinement on a non-adhesive surface, Vinculin-GFP was homogeneously distributed in the cytoplasm, and no stress fibers could be observed. Instead, actin filaments assembled into a fibrous cortex that was absent from the cell front, but became progressively denser toward the cell rear at the uropod (Figure 6A, middle panel; Movie S6). Myosin II formed patches in A2 cells, mostly on the rear part of the cell where the actin cortex was denser. Both actin filaments and myosin II patches showed a strong retrograde flow in the central part of the cell ($15.8 \pm 3.7 \mu\text{m}/\text{min}$ SD $n = 11$, measured in the reference frame of the cell), whereas almost no actin movement was observed in the rear of the cell and in the uropod (Figure 6A bottom panel; see also Movie S7 and Figure 6B for flow visualization by particle image velocimetry).

To assess whether A1 motility relied on a similar mechanism, we added 30 μM of the ROCK inhibitor Y27632. As with the A2 cells, we found that motile single A1 cells displayed a fast retrograde flow ($14.63 \pm 0.9 \mu\text{m}/\text{min}$). Unlike the A2 cells, however, the flow was not global, from the front to the back of the cell. Instead, it was localized only in a small protruding region at the leading edge of the cell (Figures S6A and S6B; Movie S8). The limited area of the retrograde flow might explain why these cells were slower than A2 cells.

Several studies have shown that such a retrograde flow is responsible for cell movement independently of adhesion in amoeboid cells (Bergert et al., 2012; Renkawitz et al., 2009). To confirm the role of the retrograde flow in cell movement, we also compared retrograde flow speed with cell speed and found a significant correlation between these two parameters (Figure S6E). However, retrograde flow was faster than the cell speed, indicating that a limited amount of friction occurs between the flowing cortex and the substrate surface (Renkawitz et al., 2009). In A2 cells lacking a uropod, the cell could go as fast as the retrograde flow (Figure S6F; Movie S8), and on average, A2 cells were 1.84 time faster (1.32–2.58 at 95% confidence) after being detached from their uropod (see also Figures S6C and S6D). These results confirmed that A2 cells moved via a coupling of a fast acto-myosin retrograde flow with the substrate and that the uropod acted as a dragged passive body.

Figure 4. Strong Confinement in a Non-Adhesive Environment Can Induce Two Distinct Modes of Amoeboid Migration

(A) Time-lapse sequences of a typical amoeboid RPE1 (left) and HeLa VL (right) cell under 3- μm confinement on a non-adhesive PEG surface. Grey is phase contrast and blue is nuclear staining (Hoechst). Time is in min ('). Scale bar represents 20 μm .

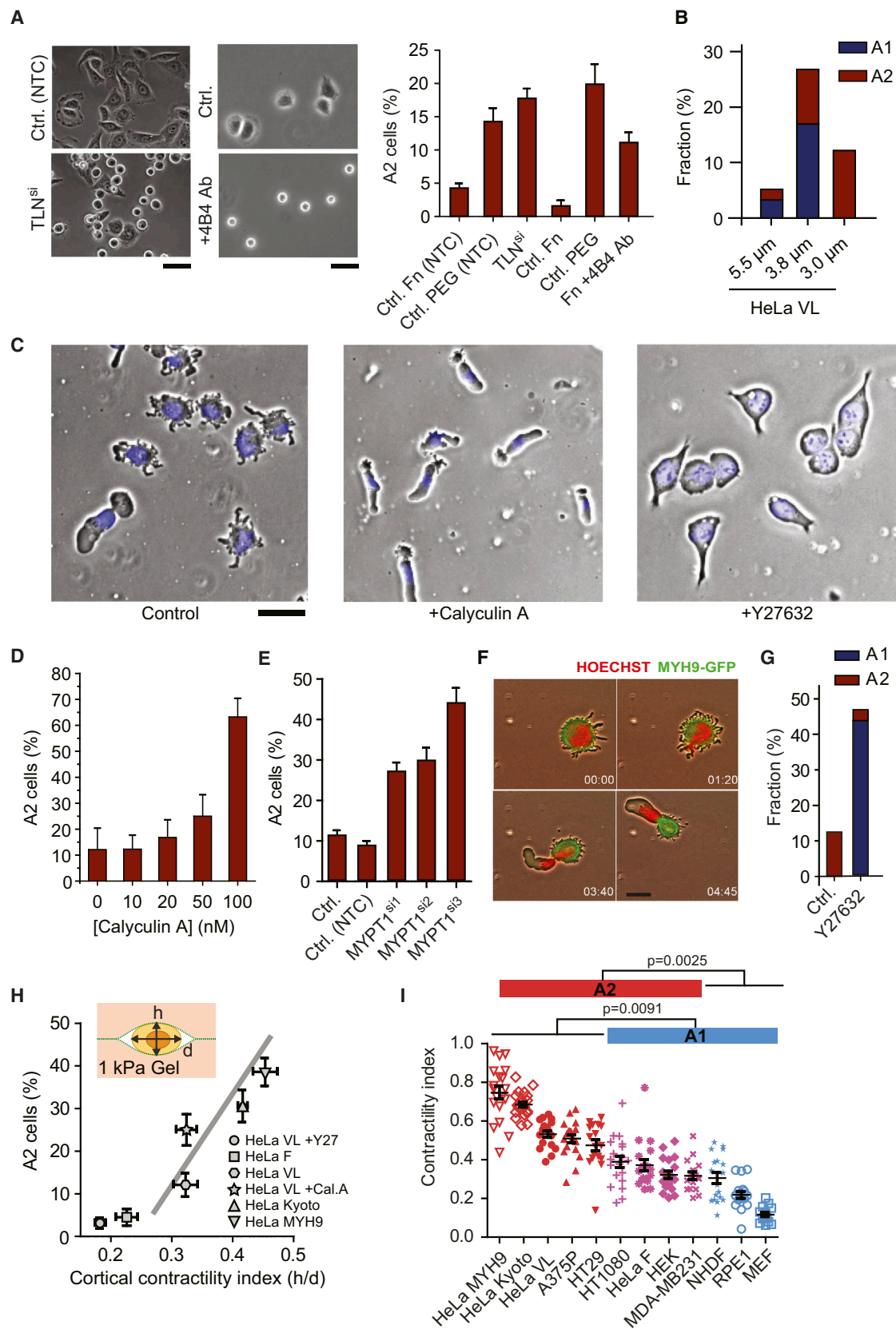
(B) Fraction of each phenotype for various cell lines under 3- μm confinement on a non-adhesive surface ($n = 140, 147, 267, 129, 60, 138, 137, 115$, and 112 cells).

(C) Instantaneous migration speed for various cell lines depending on their migratory phenotype ($n = 13, 13, 13, 13, 13, 22, 6, 10, 11, 10, 2, 9, 3, 10, 46$, and 11).

* $p < 0.05$, ** $p < 0.01$ according to t test.

(D) Comprehensive table indicating the presence or absence of amoeboid phenotypes for various cell lines: blue indicates RPE1-like (A1), red indicates HeLa-like (A2), purple indicates both (A1+A2), and gray indicates none. Cells are sorted by their origins and state of transformation. Species are human (h), mouse (m), and dog (d). Origins are primary (p), immortalized (i), and tumoral (t).

See also Figure S4 and Movie S3.



(legend on next page)

In A2 Cells, the Stable and Global Retrograde Flow Is Induced by Myosin II Contractility and Asymmetrical Actin Turnover

To better understand how global retrograde flow could be maintained and how actin was recycled in the cell, we calculated the polymerization dynamics of filamentous actin. We first measured the 1D retrograde flow of actin and myosin II along the length of cells (see [Extended Experimental Procedures](#) for details). In individual cells, the mean rate of flow (in the reference frame of the moving cell) was similar for both proteins ([Figure 6C](#)). In terms of protein localization, however, myosin II patches appeared to lie further toward the back of the cell ([Figure 6D](#); [Movie S6](#)). Interestingly, we noticed that myosin II was localized where the actin retrograde flow accelerated ([Figure 6D](#), bottom-right graph) and that the gradient of speed of the actin filaments, which accounts for the actin network contraction, was similar to the mean myosin II density along the cell ([Figure 6D](#)). This suggested a role for myosin II in accelerating the retrograde actin flow.

To produce a stable cortical flow, cortical actin has to be recycled. According to the well-accepted model for actin filament turnover ([Wilson et al., 2010](#)), new actin monomers are polymerized at the cell front and filamentous actin is severed at the back of the cell. As in [Wilson et al. \(2010\)](#), we were able to use the mass conservation law to deduce the rate of polymerization of filamentous actin along the cell length (see [Supplemental Information](#) for details). We found that actin polymerized at the front at a constant rate and depolymerized at the back ([Figure 6E](#)). A similar analysis of myosin II dynamics showed that recruitment of this protein was reduced toward the cell front, suggesting that it was rapidly captured by actin filaments and moved toward the rear of the cell.

Based on these elements, a mathematical model can be proposed (summarized in [Figure 6H](#) and [Supplemental Information](#)) (see also [Ruprecht et al. \[2015\]](#) in this issue of *Cell*; [Callan-Jones and Voituriez, 2013](#); [Hawkins et al., 2011](#)), which predicts

appearance of a motile “stable bleb” state above a threshold of contractility of the acto-myosin cortex.

To further test this model, we assessed the respective roles of actin turnover and myosin II contractility in A2 migrating cells. When cells were treated with low concentrations of jasplakinolide, a drug that interferes with actin filament turnover, an increasing fraction of the actin filaments was found to accumulate at the cell back ([Figure 6F](#)). Above 250 nM, the proportion of A2 cells dropped ([Figure 6F](#)). Treated cells also displayed an unstable and floppy front, showing that cortex turnover was essential for the stability of the A2 mode. To test the role of myosin II during steady-state migration, we introduced the drug into the device after the A2 cells had formed. After treatment, cells concomitantly lost their elongated shape to become round and stopped moving ([Figure 6G](#)). Myosin II activity was thus not only required for spontaneous polarization, but also, together with actin filament turnover, to maintain the cortical flow, the shape, and the motility of the A2 mode.

All these observations are consistent with our model and are identical to the observations made on embryonic fish cells reported by [Ruprecht et al. \(2015\)](#) in this issue of *Cell*. This suggests a common generic mechanism for the migration of contractile confined cells which are not able to form acto-myosin stress fibers and instead form a contractile cortex. When a cell exceeds a certain level of contractile activity, its cortex can be destabilized by blebs and switch spontaneously to another stable state that induces a fast migration behavior ([Figure 6I](#)). Conversely, when a cell is only moderately contractile, its cortex is constantly being destabilized by blebs but does not switch to a new stable configuration, leading to non-migrating, blebbing cells. When contractility is completely inhibited, the cortex is not destabilized, and a cell can develop more protrusive activity, which eventually leads to the A1 type amoeboid-like migration.

Figure 5. Migratory Transitions Depend on Myosin II Activity and on the Presence of Focal Adhesions

(A) Left panel: representative images of HeLa VL on a fibronectin-treated substrate after treatments against adhesion: by Talins depletion (TLN1+TLN2) with siRNA compared with a non-targeting control (NTC) or by blocking $\beta 1$ integrins with the 4B4 antibody (30 $\mu\text{g}/\text{ml}$). Right panel: fraction of A2 cells after confinement on a non-adhesive surface (PEG) or a fibronectin-coated surface (Fn) with or without treatments against focal adhesions ($n = 482, 313, 687, 240, 424$, and 436 cells). Scale bar represents 50 μm . All confined cells are under 3- μm confinement and error bars are either SEM for means or error margin for %.

(B) Fraction of each phenotype for HeLa VL cells depending on confinement level on a non-adhesive PEG surface ($n = 308, 254$, and 140 cells). All confined cells are under 3- μm confinement and error bars are either SEM for means or error margin for %.

(C) Representative images of HeLa VL cells without and with 100 nM calyculin A or 30 μM Y27632 treatments under 3- μm confinement on a non-adhesive PEG surface. Scale bar represents 50 μm . All confined cells are under 3- μm confinement and error bars are either SEM for means or error margin for %.

(D) Fraction of A2 cells for various calyculin A concentrations, in HeLa VL cells ($n = 140, 327, 208, 140$, and 185 cells). All confined cells are under 3- μm confinement and error bars are either SEM for means or error margin for %.

(E) Fraction of HeLa VL cells transitioning to the A2 phenotype after MYPT1 depletion with three distinct sequences of siRNAs or after a non-targeting control (NTC) treatment ($n = 664, 637, 408, 211$, and 177 cells). All confined cells are under 3- μm confinement and error bars are either SEM for means or error margin for %.

(F) Time-lapse sequences of a HeLa Kyoto cell showing transition from a rounded blebbing cell (phenotype B) to A2 phenotype. Images are an overlay of phase contrast (gray), MYH9-GFP fluorescence (green, staining myosin II), and Hoechst nuclear staining (red). Time is in hr:min. Scale bar represents 25 μm .

(G) Fraction of HeLa VL cells transitioning to A1 and A2 phenotypes after 30 μM Y27632 treatment ($n = 140$ and 191 cells). All confined cells are under 3- μm confinement and error bars are either SEM for means or error margin for %.

(H) For various HeLa clones or after treatment with Y27632 (30 μM) or calyculin A (50 nM), fraction of A2 cells compared with the mean contractility index of cells $\langle h/d \rangle$, which quantifies the ability of detached cells to deform a soft non-adhesive polyacrylamide (PA) gel of 1 kPa. For each point: $n > 200$ cells on y axis and $n > 15$ on x axis.

(I) Contractility index of various cell types showing either A1 or A2 migration ($n = 19, 22, 18, 20, 17, 19, 18, 19, 17, 18, 17$, and 15 ; p values are from a non-parametric Mann-Whitney test).

See also [Figure S5](#) and [Movies S4](#) and [S5](#).

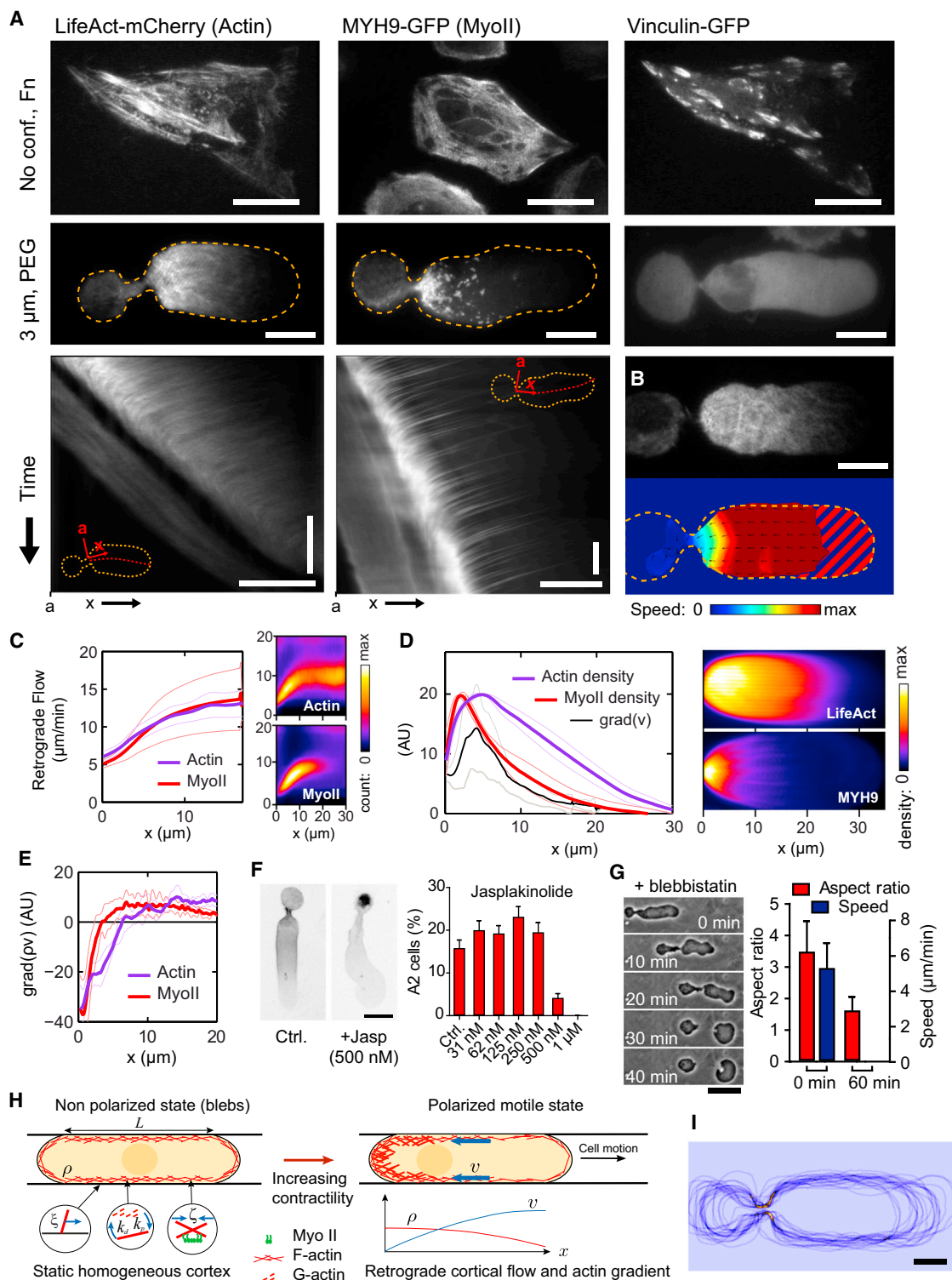


Figure 6. Motility of A2 Fast-Moving Phenotype Is Based on a Strong Actin Retrograde Flow

(A) Representative TIRF microscopy images of HeLa cells expressing both Vinculin-GFP (left) and LifeAct-mCherry (right) (HeLa VL), and HeLa cells expressing MYH9-GFP (middle) under the following two conditions: on fibronectin-coated adhesive surface without confinement (top panel) and confined under 3 μm on a non-adhesive PEG surface (middle panel). Bottom images correspond to kymographs showing retrograde flow in the cell body. Orange dashed lines show cell outlines, red dashed lines were used to generate kymographs. Horizontal bars are 10 μm and vertical bars are 2 min.

(legend continued on next page)

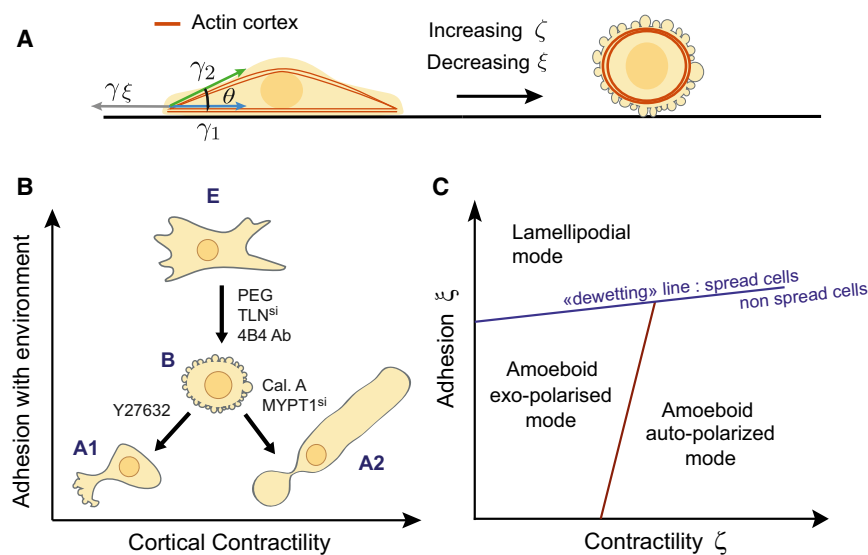


Figure 7. Schematic of the Proposed Model Describing Transitions between Modes of Cell Migration

(A) Increasing cortical tension and decreasing cortex-surface interaction both converge toward a round, “non-wetting” shape of the cell.
(B) Summary of experimental observations.
(C) Generic phase diagram resulting from models of cortical wetting and cortical stability.

hesions. We found that when cells were still able to form focal adhesions, they formed persistent protrusions and stress fibers, all of which prevented the formation of large-scale cortical flows. This observation is consistent with previous reports that integrin expression inhibits amoeboid migration (Carragher et al., 2006). Focal adhesions and the cell cortex might compete to re-

DISCUSSION

A Phase Diagram of Cell Migration Can Be Drawn Based on Only Three Parameters

Amoeboid migration has been described as a fast migration mode potentially independent of adhesion and involving a rounded cell shape. However, no consensus on its mechanism has been established. Here, we showed that physical confinement and low adhesiveness could promote a mesenchymal-to-amoeboid transition across a range of cell types that have not been thought to be capable of amoeboid motility. In addition, cortical contractility determined the type of amoeboid migration, leading to a general phase diagram for single cell locomotion, based on only three main parameters: adhesion, confinement, and contractility (Figure 7B).

Below, we discuss in more detail how these three parameters, either individually or in conjunction, might contribute to the migratory transitions that we observed.

The Absence of Focal Adhesion Allows the Formation of a Cell Cortex and a Switch to a Rounded State

An intriguing aspect of the transition to amoeboid migration modes is that, in all cases, it required the absence of focal ad-

hesions. We found that when cells were still able to form focal adhesions, they formed persistent protrusions and stress fibers, all of which prevented the formation of large-scale cortical flows. This observation is consistent with previous reports that integrin expression inhibits amoeboid migration (Carragher et al., 2006). Focal adhesions and the cell cortex might compete to re-

cruit the acto-myosin contractile machinery, leading to either contractile stress fibers or a contractile/flowing cortex. In the absence of focal adhesions, cortical tension can trigger the mechanical delamination of remaining adhesive sites, leading to a rounded shape. To mathematically account for this transition from a spread, adherent phenotype to a round shape at low adhesion and high contractility, we can draw an analogy with the dewetting of liquid droplets on flat surfaces (see Supplemental Information). This qualitatively accounts for the observed transition from phenotype E to B in Figure 7. This analogy, although speculative at that stage, is useful to complete the theoretical framework recapitulating our observations. It captures the importance of the balance between contractility and adhesion.

Importantly, adhesion alone does not prevent the transition to amoeboid migration, but rather its association with the formation of stress fibers. As a consequence, cell types that could adhere to particular matrix components without generating stress fibers could also move with a flowing cortex, leading to amoeboid migration even in the presence of a strong coupling between the actin cortex and the cell environment. This type of motility has been observed in leukocytes, in cancer cells invading a soft non-crosslinked matrix such as Matrigel (Poincloux et al.,

(B) Particle image velocity (PIV) of actin flows (bottom image) recorded on a TIRF movie (top image). Dashed part corresponds to areas where signal was too weak for flow calculation. Scale bar represents 10 μm .

(C) Mean retrograde flow along the cell (in the reference frame of the cell). Right images show speed distribution measured for 15 min on an individual cell and left graph shows mean flow averaged over several cells. $x = 0$ corresponds to the position of the neck.

(D) Mean actin (based on LifeAct staining) and myosin II density profiles. Right images show 2D mean densities in the cell body averaged for 15 min on a single cell and left graph shows mean density profile for several cells. myosin II density colocalized with actin retrograde flow gradient $\text{grad}(v)$.

(E) Polymerization rates estimates along the cell body for myosin II and actin. Inferred from density and retrograde flow profiles shown in (C) and (D).

(F) Left: actin localization (inverted image of LifeAct fluorescence) in a HeLa VL A2 cell with or without jasplakinolide treatment. Right: fraction of A2 cell function of jasplakinolide concentration (for each bar $n > 278$ cells, error bars are error margins). Scale bar represents 20 μm .

(G) Time-lapse sequence of a A2 HeLa VL cell after a 150 μM blebbistatin treatment (left) and quantification of the aspect ratio of the cell front and cell speed before and 60 min after treatment ($n = 7$ cells, error bars are SEM) (right). 3- μm confinement, PEG. Scale bar represents 50 μm .

(H) Schematic of the proposed model for cell motion (see main text and Supplemental Information).

(I) Mean cell shape: superposition of the outlines of 22 cells showing the reproducibility and stability of cell shape in mode A2. Scale bar represents 10 μm . In (C)–(E), $n = 5$ (actin), six (myosin II) cells, error envelop is SEM and 0 on x axis corresponds to the neck position. Point a in (A).

See also Figure S6 and Movies S6, S7, and S8.

2011), and in embryonic cells from zebrafish (Ruprecht et al. [2015] in this issue of *Cell*).

Confinement Is Required for Transmission of Forces in the Absence of Adhesion, but It Also Increases Contractility

When mesenchymal cells are prevented from forming focal adhesions, they cannot hold on to fibronectin- or collagen-coated substrates. This automatically makes confinement a requirement for cell migration. This phenomenon has been termed “chimneying” (Malawista et al., 2000), in reference to a technique used by mountain climbers. Exactly how these frictional forces are transmitted from the acto-myosin cortex to the migration substratum remains an open question. In addition, it has been proposed that confinement, in more complex geometries, combined with blebbing activity and an intrinsic cell polarity, could allow complete non-frictional motion to occur (Tozluoğlu et al., 2013). In conclusion, the most direct function of confinement is to enable force transmission in the absence of adhesions to the substrate.

An unexpected effect of confinement was to significantly increase contractility, thus favoring blebbing and the A2 mode of migration. As this effect was immediate, it could not rely on the activation of a transcriptional program. Force-induced signaling via focal adhesions could not explain this effect either, as cells did not form adhesive structures. This suggests that the increase in contractility observed upon confinement might be induced directly by cell and/or nuclear deformation through a yet-unknown mechanism.

A Major Difference between A1 and A2 Migration Modes Is the Origin of the Polarization Process that Triggers Cell Movement

An intrinsic polarization factor or process in the cell, or an extrinsic spatial cue can induce a local retrograde flow in a protrusive structure (Lorentzen et al., 2011). Indeed, we observed that cells switched to the A1 migration mode after making contact with cell debris or with other cells, or after a division. This indicated that this mode of migration only rarely appeared spontaneously and relied on a polarization factor to locally trigger the retrograde flow and thus the cell movement.

Cell polarity can also be induced in the absence of a specific polarization signal, a phenomenon previously described in other studies (Lorentzen et al., 2011; Poincloux et al., 2011). We found that this spontaneous polarization of a contractile cell cortex, which is predicted by our minimal model based on active gel theory (see Supplemental Information), can be nucleated randomly by the blebbing activity (see also Ruprecht et al. [2015] in this issue of *Cell*). Following destabilization of the cortex and transfer of the cytoplasm to the large bleb, contractility remains concentrated at the back of the cell due to the global flow, generating a stabilizing feedback. This can trigger an increase in pressure in the cell, a phenomenon reminiscent of lobopodial migration (Petrie et al., 2012, 2014). The movement of the global actin retrograde flow can also be transmitted to the substratum.

This phenomenon of a steady-state flow based on actin filament turnover is essentially similar to the mechanism driving pro-

trusive lamellipodial migration (Wilson et al., 2013) or A1 cell motility. But, importantly, while A1 motility requires an additional mechanism for polarization, in the case of high contractility (A2 mode), we provided evidence, both theoretical and experimental, that a stable polarization and thus a persistent migration can occur spontaneously.

A2 Migration: A Generic, Ancestral Mode of Cell Locomotion?

For all cell lines studied, the speed of amoeboid-like migration was much faster than the speed of the mesenchymal form and corresponded to values reported for amoeboid cell types (several $\mu\text{m}/\text{min}$). This suggests that these typical speeds are rather linked to the mode of migration than to the type of cell, as a given cell type can adopt both types of migration and associated speed, depending on its migration environment.

While we could observe two different types of fast amoeboid migration, the A2 mode appeared to be more general. Most cell types were able to adopt it, if contractile and sufficiently confined. Strikingly, all cell lines displayed a unique shape and speed when in the A2 mode, resembling the shape of a migrating neutrophil, with a pronounced uropod and a smooth rounded leading edge and with a similar range of speed. This was independent of their tissue of origin, of their physiological function, and of the shape and speed they displayed when migrating on an adhesive substrate without confinement. Importantly, embryonic cells from zebrafish could also display the same general shape and range of speed (Ruprecht et al. [2015] in this issue of *Cell*).

When we investigated the acto-myosin dynamics underlying the migration of these cells in more detail, the similarity appeared to be even more striking. Interestingly, the stereotypical “sausage” shape of the A2/stable bleb migrating cells has also been reported for amoebae, with also a similar actin and myosin II distribution (Yoshida and Inoué, 2001). This suggests that the transition to the A2, or “stable-bleb” fast amoeboid-like migration might be a very general phenomenon, relevant not only for cultured cancer cells but also for primary embryonic cells, both in vitro and in vivo.

From a mathematical point of view, the transition to A2 migration mode can be understood with a very generic minimal 1D theoretical model. The fact that such a simple and generic model can predict the transition to A2/stable bleb migration suggests that this mode of locomotion could be viewed as a basic property of a dynamic and contractile actin cortex. Consistent with this view, we often observed cell fragments of various sizes, resulting from shedding of large blebs, moving with the same shape, speed, and actin dynamics as A2 cells.

Taken together, the generality of the A2/stable bleb migration mode, the strong conservation of its main features (cell shape, cell speed, acto-myosin distribution, and dynamics) across a variety of cell types and organisms ranging from amoebae to vertebrates, the generic aspect of the model describing it, and the key feature of spontaneous polarization, make it tempting to speculate that this mode of migration may be an ancestral locomotion mechanism for crawling cells, shared by eukaryotes.

A2 Migration Mode Is Related to Cell Transformation

An interesting result emerging from the comparison of various cell types (Figure 4D), is that the capacity to display amoeboid motility seems to correlate with the transformed character of the cells assayed. This suggests an increased migration plasticity of cancer cells.

Importantly, the various migration modes can be observed in a single cell line by slightly varying the confinement level, adhesion, and contractility. As a consequence, some physical characteristics of the tumor environment, such as the confinement imposed by the surrounding tissue on the growing tumor, might be enough to trigger a migratory switch toward a faster and more invasive mode of migration. Such an increase in the migration and invasion capacity of tumor cells has been observed using encapsulated spheroids as a model for tumor growth under confinement (Alessandri et al., 2013). This phenomenon could also explain how inhibition of matrix-degrading enzymes such as MMPs could directly promote a switch to amoeboid migration by increasing the confinement of the growing tumor and/or of single migrating cells (Wolf et al., 2003). In conclusion, our work demonstrates an unexpected plasticity of migration of transformed mesenchymal-like cells when they are not in their physiological physical environment, suggesting that tumor cells could spontaneously adopt a large variety of strategies to escape primary tumors and invade tissues, without any specific genetic alteration.

EXPERIMENTAL PROCEDURES

In brief (see Supplemental Information for a detailed description of the methods), cell culture and experiments were performed in complete cell culture media adapted for each particular cell type. Drugs and RNAi treatments were performed following standard procedures. Cell confinement was performed using a home-made device (Le Berre et al., 2012) consisting of a suction cup made in polydimethylsiloxane (PDMS, RTV615, GE) used to press a confining coverslip bearing PDMS micro-spacers on top of the culture substrate platted with cells. Alternatively, a version of the cell confiner adapted to multi-well plates was used to perform multiple experiments in parallel. The molds for the PDMS micro-spacers were fabricated following standard photolithography procedures. The surface of the confining side was always treated with non-adhesive pLL-PEG (SuSoS), while the cell culture substrate was treated to obtain various degrees of cells adhesion using mixes of pLL-PEG and pLL-PEG-RGD. For automated cell tracking, cell nuclei were stained with Hoechst 33342. Image acquisition and image analysis were performed on workstations of the PICT-IBISA Lhomond Imaging facility of Institut Curie. All microscopes used for time-lapse recordings were equipped with an on-stage incubation chamber which maintained the temperature at 37°C and CO₂ concentration at 5% at all times. Image analysis was performed using Image J or MetaMorph software (Universal Imaging), or homemade routines under MATLAB (Math-Works). Analysis of cell trajectories was based on standard methods for analysis of persistent random walks. To measure single cell contractility index, cells were plated between two poly-acrylamide gels coated with beads and the cell dimensions as well as the gel deformation were measured by confocal microscopy. HeLa VL cells were always used as a reference for gel calibration. A minimal 1D theoretical model, based on the observations of the acto-myosin flows analysis, was adapted from Callan-Jones and Voituriez (2013) and Hawkins et al. (2011) to predict the mesenchymal to amoeboid transition.

SUPPLEMENTAL INFORMATION

Supplemental Information includes Extended Experimental Procedures, six figures, and eight movies and can be found with this article online at <http://dx.doi.org/10.1016/j.cell.2015.01.007>.

AUTHOR CONTRIBUTIONS

Y.-J.L. designed and carried out a majority of the experiments, performed data analysis, made the figures, and contributed to writing the paper. M.L.-B. carried out experiments, performed a majority of the data analysis, supervised the work, and wrote the paper. F.L. performed some TIRF experiments. P.M. carried out some data analysis. M.H. and T.T. performed immunoblotting. A.C.J. and R.V. made the physical model. M.P. designed experiments, supervised the work, and wrote the paper.

ACKNOWLEDGMENTS

The authors acknowledge the Nikon Imaging Centre at the Institut Curie-CNRS and Vincent Fraissier from the PICT-IBISA Lhomond Imaging facility of Institut Curie for their help with the microscopy, and Timo Betz for kindly sharing his software for PIV analysis. We thank Stéphanie Miserey-Lenkei and Nicolas Carpi for their help with western blots. Vivatch and ARC are acknowledged for their financial support to Y.-J.L. and M.L.B., ANR-09-PIRI-0027 and InNaBioSanté to R.V. and M.P., and ERC 311205-PROMICO to M.P.

Received: May 2, 2014

Revised: October 31, 2014

Accepted: December 31, 2014

Published: February 12, 2015

REFERENCES

- Alessandri, K., Sarangi, B.R., Gurchenkov, V.V., Sinha, B., Kießling, T.R., Fetter, L., Rico, F., Scheuring, S., Lamaze, C., Simon, A., et al. (2013). Cellular capsules as a tool for multicellular spheroid production and for investigating the mechanics of tumor progression in vitro. *Proc. Natl. Acad. Sci. USA* **110**, 14843–14848.
- Barnhart, E.L., Lee, K.-C., Keren, K., Mogilner, A., and Theriot, J.A. (2011). An adhesion-dependent switch between mechanisms that determine motile cell shape. *PLoS Biol.* **9**, e1001059.
- Bergert, M., Chandradoss, S.D., Desai, R.A., and Paluch, E. (2012). Cell mechanics control rapid transitions between blebs and lamellipodia during migration. *Proc. Natl. Acad. Sci. USA* **109**, 14434–14439.
- Callan-Jones, A.C., and Voituriez, R. (2013). Active gel model of amoeboid cell motility. *New J. Phys.* **15**, 025022.
- Carragher, N.O., Walker, S.M., Scott Carragher, L.A., Harris, F., Sawyer, T.K., Brunton, V.G., Ozanne, B.W., and Frame, M.C. (2006). Calpain 2 and Src dependence distinguishes mesenchymal and amoeboid modes of tumour cell invasion: a link to integrin function. *Oncogene* **25**, 5726–5740.
- DiMilla, P.A., Stone, J.A., Quinn, J.A., Albelda, S.M., and Lauffenburger, D.A. (1993). Maximal migration of human smooth muscle cells on fibronectin and type IV collagen occurs at an intermediate attachment strength. *J. Cell Biol.* **122**, 729–737.
- Feng, J., Ito, M., Ichikawa, K., Isaka, N., Nishikawa, M., Hartshorne, D.J., and Nakano, T. (1999). Inhibitory phosphorylation site for Rho-associated kinase on smooth muscle myosin phosphatase. *J. Biol. Chem.* **274**, 37385–37390.
- Friedl, P., and Wolf, K. (2003). Tumour-cell invasion and migration: diversity and escape mechanisms. *Nat. Rev. Cancer* **3**, 362–374.
- Giampieri, S., Manning, C., Hooper, S., Jones, L., Hill, C.S., and Sahai, E. (2009). Localized and reversible TGF β signalling switches breast cancer cells from cohesive to single cell motility. *Nat. Cell Biol.* **11**, 1287–1296.
- Hawkins, R.J., Piel, M., Faure-Andre, G., Lennon-Dumenil, A.-M., Joanny, J.F., Prost, J., and Voituriez, R. (2009). Pushing off the walls: a mechanism of cell motility in confinement. *Phys. Rev. Lett.* **102**, 058103.
- Hawkins, R.J., Poincloux, R., Bénichou, O., Piel, M., Chavrier, P., and Voituriez, R. (2011). Spontaneous contractility-mediated cortical flow generates cell migration in three-dimensional environments. *Biophys. J.* **101**, 1041–1045.
- Heuzé, M.L., Vargas, P., Chabaud, M., Le Berre, M., Liu, Y.-J., Collin, O., Solanes, P., Voituriez, R., Piel, M., and Lennon-Dumenil, A.-M. (2013). Migration of

dendritic cells: physical principles, molecular mechanisms, and functional implications. *Immunol. Rev.* 256, 240–254.

Hung, W.-C., Chen, S.-H., Paul, C.D., Stroka, K.M., Lo, Y.-C., Yang, J.T., and Konstantopoulos, K. (2013). Distinct signaling mechanisms regulate migration in unconfined versus confined spaces. *J. Cell Biol.* 202, 807–824.

Ishihara, H., Martin, B.L., Brautigan, D.L., Karaki, H., Ozaki, H., Kato, Y., Fuse-tani, N., Watabe, S., Hashimoto, K., Uemura, D., et al. (1989). Calyculin A and okadaic acid: inhibitors of protein phosphatase activity. *Biochem. Biophys. Res. Commun.* 159, 871–877.

Lämmermann, T., and Sixt, M. (2009). Mechanical modes of ‘amoeboid’ cell migration. *Curr. Opin. Cell Biol.* 21, 636–644.

Lämmermann, T., Bader, B.L., Monkley, S.J., Worbs, T., Wedlich-Söldner, R., Hirsch, K., Keller, M., Förster, R., Critchley, D.R., Fässler, R., and Sixt, M. (2008). Rapid leukocyte migration by integrin-independent flowing and squeezing. *Nature* 453, 51–55.

Le Berre, M., Aubertin, J., and Piel, M. (2012). Fine control of nuclear confinement identifies a threshold deformation leading to lamina rupture and induction of specific genes. *Integr. Biol. (Camb)* 4, 1406–1414.

Lorentzen, A., Bamber, J., Sadok, A., Elson-Schwab, I., and Marshall, C.J. (2011). An ezrin-rich, rigid uropod-like structure directs movement of amoeboid blebbing cells. *J. Cell Sci.* 124, 1256–1267.

Malawista, S.E., de Boisfleury Chevance, A., and Boxer, L.A. (2000). Random locomotion and chemotaxis of human blood polymorphonuclear leukocytes from a patient with leukocyte adhesion deficiency-1: normal displacement in close quarters via chimneying. *Cell Motil. Cytoskeleton* 46, 183–189.

Paluch, E.K., and Raz, E. (2013). The role and regulation of blebs in cell migration. *Curr. Opin. Cell Biol.* 25, 582–590.

Panková, K., Rösel, D., Novotný, M., and Brábek, J. (2010). The molecular mechanisms of transition between mesenchymal and amoeboid invasiveness in tumor cells. *Cell. Mol. Life Sci.* 67, 63–71.

Petrie, R.J., Gavara, N., Chadwick, R.S., and Yamada, K.M. (2012). Nonpolarized signaling reveals two distinct modes of 3D cell migration. *J. Cell Biol.* 197, 439–455.

Petrie, R.J., Koo, H., and Yamada, K.M. (2014). Generation of compartmentalized pressure by a nuclear piston governs cell motility in a 3D matrix. *Science* 345, 1062–1065.

Poincloux, R., Collin, O., Lizárraga, F., Romao, M., Debray, M., Piel, M., and Chavrier, P. (2011). Contractility of the cell rear drives invasion of breast tumor cells in 3D Matrigel. *Proc. Natl. Acad. Sci. USA* 108, 1943–1948.

Renkawitz, J., Schumann, K., Weber, M., Lämmermann, T., Pflücke, H., Piel, M., Polleux, J., Spatz, J.P., and Sixt, M. (2009). Adaptive force transmission in amoeboid cell migration. *Nat. Cell Biol.* 11, 1438–1443.

Ruprecht, V., Wieser, S., Callan-Jones, A., Smutny, M., Morita, H., Sako, K., Barone, V., Ritsch-Marte, M., Sixt, M., Voituriez, R., and Heisenberg, C.-P. (2015). Cortical contractility triggers a stochastic switch to fast amoeboid cell motility. *Cell* 160, this issue, 674–686.

Sahai, E., and Marshall, C.J. (2003). Differing modes of tumour cell invasion have distinct requirements for Rho/ROCK signalling and extracellular proteolysis. *Nat. Cell Biol.* 5, 711–719.

Sanz-Moreno, V., and Marshall, C.J. (2010). The plasticity of cytoskeletal dynamics underlying neoplastic cell migration. *Curr. Opin. Cell Biol.* 22, 690–696.

Taddei, M.L., Giannoni, E., Comito, G., and Chiarugi, P. (2013). Microenvironment and tumor cell plasticity: an easy way out. *Cancer Lett.* 341, 80–96.

Tozluoğlu, M., Tournier, A.L., Jenkins, R.P., Hooper, S., Bates, P.A., and Sahai, E. (2013). Matrix geometry determines optimal cancer cell migration strategy and modulates response to interventions. *Nat. Cell Biol.* 15, 751–762.

Trache, A., and Meininger, G.A. (2008). Total internal reflection fluorescence (TIRF) microscopy. In *Current Protocols in Microbiology*, R. Coico, T. Kowalik, J. Quarles, B. Stevenson, and R. Taylor, eds. (John Wiley & Sons).

Wilson, C.A., Tsuchida, M.A., Allen, G.M., Barnhart, E.L., Applegate, K.T., Yam, P.T., Ji, L., Keren, K., Danuser, G., and Theriot, J.A. (2010). Myosin II contributes to cell-scale actin network treadmill through network disassembly. *Nature* 465, 373–377.

Wilson, K., Lewalle, A., Fritzsche, M., Thorogate, R., Duke, T., and Charras, G. (2013). Mechanisms of leading edge protrusion in interstitial migration. *Nat. Commun.* 4, 2896.

Wolf, K., Mazo, I., Leung, H., Engelke, K., von Andrian, U.H., Deryugina, E.I., Strongin, A.Y., Bröcker, E.-B., and Friedl, P. (2003). Compensation mechanism in tumor cell migration: mesenchymal-amoeboid transition after blocking of pericellular proteolysis. *J. Cell Biol.* 160, 267–277.

Yoshida, K., and Inouye, K. (2001). Myosin II-dependent cylindrical protrusions induced by quinine in Dictyostelium: antagonizing effects of actin polymerization at the leading edge. *J. Cell Sci.* 114, 2155–2165.

EXTENDED EXPERIMENTAL PROCEDURES

Reagents

pLL(20)-g[3.5]-PEG(2) (pLL-PEG) and pLL(20)-g[3.5]-PEG(2)/PEG(3.4)-RGD (pLL-PEG-RGD) are from SuSoS. Hoechst 33342, jasplakinolide, blebbistatin, and calyculin A were purchased from Sigma-Aldrich, Y27632 from Calbiochem. Alex Fluor 488 and Alex Fluor 594 were purchased from Invitrogen. All other reagents were purchased from Sigma-Aldrich unless otherwise specified.

Cell Culture, Staining, and Sample Preparation

Normal Human Dermal Fibroblasts (NHDF) cells from human abdominal skin (Biopredic) and RPE1 (Human, Retinal Pigment Epithelial) cells expressing LifeAct-mCherry were cultured in DMEM/F-12 medium (GIBCO) supplemented with 10% fetal calf serum (FCS; biowest), 2 mM glutamine (GIBCO). Normal Human Epidermal Keratinocytes (NHEK) were cultured in EpiLife medium (GIBCO) complemented with HKGS Keratinocyte supplement (GIBCO). MCF10A cells (Human breast, epithelial) were cultured in DMEM/F12 with 5% Horse serum, 20 ng/mL EGF, 0.5 mg/mL Hydrocortisone, 100 ng/mL Cholera Toxin and 10 μ g/mL insulin. HeLa VL (Human, cervix) expressing Vinculin-GFP and LifeAct-mCherry (Riedl et al., 2008), HeLa Kyoto expressing MYH9-GFP (kindly provided by Ina Poser (Poser et al., 2008)), HeLa F cells (fast moving HeLa subclone, kindly provided by Franck Perez), MEF (Mouse Embryonic Fibroblasts), MDA-MB231 (Human breast adenocarcinoma, epithelial) and HT29 (Human colon adenocarcinoma, kindly provided by Danijela Vignjevic), A375P and A375M2 (Human melanoma, kindly provided by Erik Sahai), HT1080 (Human fibrosarcoma), MDCK (Dog, kidney, epithelial), C2C12 (Mouse myoblast) and HEK293 (Human, embryonic kidney, transformed by adenovirus), were all cultured in DMEM/Glutamax (GIBCO) supplemented with 10% fetal calf serum (FCS; Biowest) supplemented with antibiotics (penicillin and streptomycin, PeSt; GIBCO) at 37°C in a humidified atmosphere containing 5% CO₂. All cells were cultivated with antibiotics (1% penicillin and streptomycin mix (PeSt; GIBCO) and cells expressing a plasmid were selected with G418 (0.5 mg/mL) or puromycin (0.33 μ g/mL) (Calbiochem). All cells were dissociated Trypsin-EDTA (GIBCO) or Trypsin express (GIBCO).

For typical mesenchymal NHDF migration behavior studies, NHDF cells were seeded at a density of 4×10^3 cells/cm² on 35 mm petri dishes with various percentages of pLL-PEG-RGD-functionalized bottom surfaces. Cells were allowed to attach overnight. To alter the density of the RGD peptides on a particular substrate, we altered the ratio of pLL-PEG-RGD to pLL-PEG in the solutions we applied to it, while maintaining the total concentration of both solutes constant (500 μ g/mL in HEPES buffer, pH 7.4). We checked the relative adsorption of these two molecules on the surface by radiometric quantification of Alex 488-labeled pLL-PEG-RGD and Alex 594-labeled pLL-PEG and found that the concentration of pLL-PEG-RGD on the surface correlated almost linearly with its concentration in the solution (Figure S1C).

Before experiments were carried out, non-attached cells and floating cells were removed by extensive washing with $1 \times$ PBS and attached cells nuclei were stained in DMEM/F-12 cell culture medium containing 40 ng/mL Hoechst 33342 for 1 hr at 37°C. Cells were squeezed with the one-well cell confiner for NHDF with non-adhesive micro-structured slides bearing spacers of thicknesses ranging from 2.8 μ m to 15 μ m (Figure S1A). For other experiments, all cell lines were either seeded at a high density (5×10^5 cells/well) in multi-well plate with a glass bottom (MatTek) treated with pLL-PEG or seeded at a low density (4×10^3 cells/cm²) on a surface treated with 25 μ g/mL fibronectin and squeezed with the multi-well plate cell confiner (Figure S1B).

Fabrication of the Cell Confiner

Two cell confiners, one-well and multiple-well confiners, used in this work were developed in our lab (Le Berre et al., 2012) (the method is described in detail in Le Berre et al. [2014]). The one-well cell confiner was composed of a suction cup and a structured confining glass slide, and can be used on a standard 35 mm petri dish compatible with high resolution microscopy (Figure S1A). Briefly, a suction cup was made in a polydimethylsiloxane (PDMS, RTV615, GE) mixture (10/1 w/w PDMS A/crosslinker B) in a custom-made mold and baked on an 80°C hot plate for 1h before unloading. The confining structure on the glass slide was made in PDMS from molds fabricated by standard photolithography. Briefly, an SU8 2005 photoresist (Microchem) was used to fabricate the mold on a silicon wafer with a regular holes array (diameter: 440 μ m, 1 mm spacing), following the manufacturer's protocol. The mold was treated with trimethylchlorosilane (TMCS) for 3 min by evaporation. Afterward, a drop of PDMS mixture (8/1 w/w PDMS A / crosslinker B) was poured into the SU8 mold. Then, a 10 mm standard microscope coverslip, freshly activated for 2 min in a plasma chamber (Harrick Plasma, Ithaca, NY, USA), was pressed on a PDMS drop to get a residual PDMS layer of minimal thickness. After baking at 95°C on a hot plate for 15 min, excess PDMS was removed. To peel off the glass slide with PDMS pillars, a drop of isopropanol was poured on the slide. Finally, the slide was gently raised by inserting a razor blade between the slide and the mold, allowing the confining glass slides bound to the PDMS structures to be lifted away. A multi-well plate confiner was designed to confine cells under various conditions in parallel (Figure S1B). The modified cover lid of a multi-well plate was used to apply confining slides to cells. In this case, large PDMS pillars were stuck on the cover lid of the multi-well plate to hold confining slides. When the lid was closed, the pillars pushed the confining slides onto the culture substrate and confined the cells. Multiple wells can be processed simultaneously and a larger surface of confining slides can be used. The process of fabrication and handling is as follows: first, large PDMS pillars were fabricated by pouring a PDMS mixture (A:B = 35:1) into a custom-made mold, removing bubbles under vacuum, baking overnight at 80°C, and getting the pillars out of the mold with the help of small amount of isopropanol. Due to the low ratio of component B in the PDMS mixture, the pillars were soft and sticky after unloading and cleaning. Second, gel-film sheets (100 μ m thickness, Gel-Pak) were positioned on the cover lid, and the large PDMS pillars were bound to the gel-film sheet so they were

positioned on top of the center of each well. Before squeezing the cells, the multi-well lid modified with large PDMS pillars was sterilized with 70% ethanol; confining slides were coated with 0.5 mg/mL pLL-PEG for 1 h in 10 mM pH 7.4 HEPES buffer, and then incubated in cell culture medium to equilibrate the PDMS.

Labeling of pLL-PEG and pLL-PEG-RGD

1 mg of pLL-PEG or pLL-PEG-RGD was dissolved in 100 mM pH 8.5 NaHCO₃ buffer. 50 μ l 1 mg/mL Alex-594 and Alex-488 were added in pLL-PEG and pLL-PEG-RGD solution respectively and reacted for 2 h at room temperature under agitation. Solutions were then dialyzed for 48 h at 4°C against 1 \times PBS to remove unreacted Alex-594 or Alex-488 (Slide-A-Lyzer MWCO 3500, Pierce).

Drug and siRNA Treatment

HeLa VL cells expressing Vinculin-GFP and LifeAct-mCherry were incubated with 10–100 nM calyculin A for 1 h in cell culture medium before image acquisition, or treated with 30 μ M Y27632 or 30 nM-1 μ M jasplakinolide all the time during image acquisition. For blebbistatin experiments (Figure 6G), cells were recorded 10 min after 5 h confinement, then medium around the pillars was replaced 3 times consecutively with medium containing 150 μ M blebbistatin. A high dose of blebbistatin was used since PDMS absorb the drug. For the RNAi experiments, cells were transfected with RNAiMAX (Life Technologies) using standard concentrations provided by the manufacturer for transfection mixes made in Optimem medium (GIBCO). 40000 cells suspended in 250 μ l of antibiotic-free medium were then mixed with 80 μ l of transfection mix and seeded in a 12-well plate coated with fibronectin (25 μ g/mL in PBS). After 48 h incubation, cells were re-suspended in their standard medium and processed for the experiment.

RNAi sequences were GGAAUUAACAGGGACCUUA for TLN1, GGCCACAUAUUGAAUGCAUA for TLN2, according to Lancaster et al. (2013) and CGGAUUCACUUUCUAGAUA for MYPT1. Other MYPT1 siRNAs were Ref HSS181423 from Invitrogen (#2) and Ref D-011340 from Dharmacon (#3). To control for MYPT1 siRNA efficiency (Figure S5E), cell extracts were prepared 48 h after transfection with control siRNAs and MYPT1. TLN [8D4] antibody (ab11188 from Abcam), MYPT1 antibody (sc-25618 from Santa Cruz Biotech) and GAPDH (ab105428 from Abcam) were used for detection on the western blot. For Phospho-MLC quantification, cell were lysed at 4°C with a lysis buffer complemented with 2% phosphatase inhibitor cocktail 2 (P5726, Sigma), then Myosin Light Chain 2 rabbit polyclonal Antibody (Cell signaling #3672) was used for total MLC staining and Myosin phospho S19/phospho S20 rabbit polyclonal Antibody (Rockland #600-401-416) for Phospho-MLC staining.

Cell Migration under 2D Confinement on Controlled Adhesive Surface

Height of cells was measured by fluorescence microscopy after staining the cells with DiOC5.

For one-well cell confiner, 35 mm petri dishes were activated in a plasma chamber (Harrick Plasma, Ithaca, NY, USA) for 1 min under a weak flow of clean dry air. Then, for preparation of the various densities of RGD-coated surfaces, the dishes were immediately coated with different percentages of pLL-PEG-RGD for 1 h at room temperature, followed by three washing steps with 1 \times PBS. 4 \times 10⁴ NHDF cells were seeded into petri dishes that had been coated with different percentages of pLL-PEG-RGD, and cultured overnight. Before being confined, cells were stained with 40 ng/mL Hoechst 33342 in cell culture medium for 1 h at 37°C and then washed with regular culture medium. The side of the 10 mm confining glass slides bearing the PDMS pillars structures was cleaned with isopropanol, well-dried, treated with plasma for 1 min, and modified with 0.5 mg/mL pLL-PEG in 10 mM pH 7.4 HEPES buffer for 1 h at room temperature. After washing three times with 1 \times PBS, these confining slides were incubated in cell culture medium plus 200 ng/mL Hoechst 33342 for 1 h at 37°C. Before the cells were confined, the petri dish was placed on the microscope. The suction cup device was carefully cleaned with 70% ethanol, dried and plugged to a precise vacuum generator (VG 1006, Elveflow) to control its internal pressure. The non-structured side of the PEG-coated confining slides were cleaned and dried, and then stuck on the piston part of the suction cup. The device was carefully put over the cell culture substrate and a 3 kPa negative pressure was applied to maintain it over the cell culture substrate without confining cells (with such a pressure, the slide is maintained at 100 μ m above the cells). To confine cells, the pressure was slowly decreased to 10 kPa negative pressure to obtain the desired spacing between the slide and the cell culture substrate. For control experiments on NHDF cells, time-lapse images were recorded without confinement under the same conditions.

For the multiple-well cell confiner, the lid was placed on the multi-well plate and maintained with adhesive tape (Scotch Magic Tape, 3M), while force was applied to the lid. During this step, it is important not to move the lid laterally, to avoid damaging the cells. Cell migration was tracked and recorded by regular transmitted light, epifluorescence, or TIRF time-lapse microscopy.

Contractility Index Measurement Method

Thin layers of 1 kPa polyacrylamide (PA) gels were prepared on the bottom of a 35 mm thin glass bottom petri dish and on a 18 mm diameter coverslip. For gel fabrication, glass was first treated with pure 3-aminopropyltrimethoxysilane for 5 min, then 30 min with 400 μ l of 0.5% glutaraldehyde in PBS. To obtain gel of 1 kPa, a premix containing 2 μ l of 200 nm blue fluorescent beads (FluoSpheres, F8805, Invitrogen), 18.8 μ l of 40% acrylamide solution (161-0140, Biorad), 12.5 μ l of 2% bis-acrylamide solution (161-0142, Biorad) in 250 μ l PBS. Then, 2.5 μ l of ammonium persulfate (APS, Sigma, 10% in water) and 0.5 μ l of tetramethylethylenediamine (TMED, Sigma) was added to the premix before a 9 μ l drop of the mix was spread on the treated glass under a coverslip. After 40 min polymerization, the coverslip was removed in PBS, extensively rinsed and incubated overnight in PBS. Before experiment, the gel made on the coverslip was put on a 14 mm diameter, 2 cm high PDMS pad which was intended to apply a slight

pressure on the coverslip with its own weight. Then, both gels were incubated 30 min in medium (with a drug if used) before cells were seeded in the petri dish at a concentration of $2 \cdot 10^6$ cells/mL. After the bottom gel in the petri dish was placed on the microscope stage, the PDMS pad holding the top gel was put on the cells seeded on the bottom gel, confining cells between the two gels (Figure S5H). After 1 h of adaptation, the height of cells was measured with beads by measuring the distance between gels with focus and diameter of cells were measured on phase contrast image (Figure S5I). Contractility index was defined as h/d . Importantly, as different gels might slightly differ in stiffness, each set of confining gels was calibrated using a particular cell line (HeLa VL), then rinsed and used to measure other cell types. s.d. between experiments performed with a same set of gels was below 5%.

Live-Cell Imaging

Time-lapse recordings were acquired with 10 ×, 20 × or 40 × objectives using either an Eclipse Ti inverted microscope (Nikon) equipped with a Coolsnap HQ2 camera (Roper Scientific) controlled by MetaMorph software (Universal Imaging) or an Axio observer inverted microscope (Zeiss) equipped with a Coolsnap HQ2 camera (Roper Scientific) controlled by Axio vision software (Zeiss). Total internal Reflection (TIRF) microscopy was performed with an Eclipse Ti inverted microscope (Nikon), a Roper laser bench (laser 491 nm and 561 nm), and a Quanterm 512 SC camera mounted on a dual view (Photometrics) controlled by MetaMorph software (Universal Imaging). All microscopes were equipped with an on-stage incubation chamber which maintained the temperature at 37°C and CO₂ concentration at 5% at all times. Image analysis was performed using Image J or MetaMorph software (Universal Imaging), or homemade routines under Matlab (Mathworks).

Analysis of Cell Trajectories

All trajectories were extracted and related parameters analyzed with a bespoke Matlab script (MathWorks, USA). First, cell paths were automatically tracked from fluorescence images of the Hoechst staining (cell nuclei, see Figures S2A and S2B). Images were segmented using a watershed method and coordinates of nuclei were defined as the center of mass of the detected nuclei surfaces. Then, cell paths were tracked from one image to another using an optimization algorithm that selected the best links between images according to a set of parameters, such as the proximity and the morphological similarity of the detected nuclei (Figure S2C). Tracks having a duration of less than 50 data points (which corresponds to 2.5 hr. of migration) were eliminated from the final analyses. For analyses of specific phenotypes, recordings of each tracked cell were extracted and cell tracks were clustered manually by visual inspection of cell morphology before further analysis.

We calculated the mean Mean Square Displacement $\langle \text{MSD} \rangle$ using the overlapping intervals method (average for all cells of the average of all pairs of time points in the tracks (Dickinson and Tranquillo, 1993) (Figure S2E). In all conditions, MSD was visually similar to what is expected for a Persistent Random Walk (PRW), i.e., persistent at short time ($\langle \text{MSD} \rangle \sim t^2$) and random walker at longer time ($\langle \text{MSD} \rangle \sim t$) as expected for fibroblasts according to the literature (Gail and Boone, 1970). It was therefore analyzed using the Furth formula for persistent random walks (Stokes et al., 1991).

However, at very short times (i.e., at high frequencies), the cell nuclei did not have a continuous motion (persistent walk) as expected for a normal PRW, but jiggled randomly (Figure S2D). This phenomenon was especially visible under non-confined conditions and was not linked to a movement of the whole cell but rather to shape changes. We interpreted these motions as being the result of nucleus movements within the cell because they were linked to the movement of cytoskeletal structures. Because these movements biased the calculation of the instantaneous speed of the cell and made it difficult to fit MSD with a PRW model, we chose to filter them with a low pass filter. When considering the power spectral density of the track, we observed that nuclei moved following a white noise dominating the signal at frequencies higher than 0.05 min^{-1} (Figure S2D, inset). To remove this noise, we filtered tracks with a bilinear low pass filter having a cutoff frequency of 0.05 min^{-1} (zero shift FIR filter having Gaussian impulse response with a width at mid-height of 15 min), which removed the high-frequency noise, but did not change the path shape at the timescale of the persistence time (red line in Figure S2D).

After filtering, a PRW model (Furth Model) (Stokes et al., 1991; Selmeczi et al., 2005) was fitted on the new mean MSD(t) data with the following equation: $\text{MSD}(t) = 2 \cdot S \cdot P(t - P(1 - e^{-t/P}))$, where S is the instantaneous speed (which is fixed here as the mean of the mean instantaneous speed of cells calculated between two time points), t is the time and P is the persistence, which is here the fitted parameter (Figure S2E). For more robustness on the persistence time calculation, we resampled the MSD(t) regularly (100 points) along a log-log scale to give similar weight to all timescales. We chose to fit only the persistence and not the instantaneous speed, which, we assumed, could not be the cause of discrepancies between the data and the model. In addition, we chose a least absolute residual robust fit (LAR) weighted by the number of tracks accounted in the mean MSD(t) for each t . This allowed us to compensate for the error induced by the lower number of long tracks in the calculus of the mean MSD for large t . The diffusion coefficient D was calculated afterward with the relation $D = S^2 P/2$, according to the Furth Model (Stokes et al., 1991).

Analysis of Retrograde Flows and Density Profiles

All kymographs were produced with a custom ImageJ macro and eventually cleaned for horizontal and vertical artifactual stripes using ImageJ Fourier transform tools. 2D Particle Image Velocimetry (PIV) analysis in Figure 6B was performed as previously described (Betz et al., 2009). Retrograde flow distributions shown on Figure 6C have been calculated using registered timelapse recordings of TIRF images of a representative cell with a custom Matlab script. This script allowed us to accumulate the distribution of speed measured by a sub-pixel resolution Particle Image Velocimetry (PIV) algorithm along one dimension for all positions and frames of

a recording. Velocity profiles shown on [Figure 6C](#) correspond to the histogram maxima. Density maps of actin and myosin shown in [Figure 6D](#) are cumulated fluorescence intensities of TIRF imaging over all frames of a registered video. Density profiles shown on the graph correspond to the profile at the central axis of the cell.

The polymerization rate is given by the relation: $p = \text{div}(\rho v)$ where ρ is the actin density and v is the retrograde flow speed ([Wilson et al., 2010](#)).

Statistical Analysis

All errors indicated in the text are SEM for quantitative values or error margin for percentages. Non parametric, two tailed, Mann-Whitney t test was performed to determine whether the difference between two groups was significantly different in their mean value, or χ^2 test in their portion (using GraphPad Prism or Microsoft excel software). Linear regressions and relative confidences were calculated with the Curve fitting toolbox of Matlab (MathWorks).

Physical Modeling

Cellular Dewetting Transition

We suggest that the transition from a spread, adherent phenotype to a round shape one at low adhesion and high contractility can be qualitatively understood by analogy with dewetting of liquid droplets on flat surfaces. With notations of [Figure 7A](#), Young's equation, which expresses the force balance of the contact line, can be written:

$$\gamma_{\xi} = \gamma_1(\zeta) + \gamma_2(\zeta) \cos \theta.$$

Here γ_{ξ} denotes the adhesion strength (in units of energy per unit area). Importantly, the cortical tension $\gamma_1(\zeta)$ in the adherent part of the cortex and the cortical tension $\gamma_2(\zeta)$ in the upper non-adherent part of the cortex increase with contractility ζ . As a result, the contact angle can be written:

$$\cos \theta = \frac{\gamma_{\xi} - \gamma_1(\zeta)}{\gamma_2(\zeta)}$$

At the spread-to-round transition, the contact angle is such that $\cos \theta = -1$, which can be realized for small enough γ_{ξ} (and therefore small friction ξ) and large enough contractility ζ . This qualitatively accounts for the observed transition from phenotype E to B in [Figure 7A](#). Assuming a linear dependence $\gamma_1(\zeta) = \alpha_1 + \beta_1 \zeta$, and $\gamma_{\xi} = \alpha \xi$, the dewetting line in the plane (ζ, ξ) can be written

$$\alpha \xi = \alpha_1 - \alpha_2 + \zeta(\beta_1 - \beta_2),$$

which is the equation used in the phase diagram of [Figure 7C](#).

Minimal Model of Mesenchymal-to-Amoeboid Transition

A minimal 1D theoretical model can be adapted from ([Callan-Jones and Voituriez, 2013](#); [Hawkins et al., 2011](#)) to predict the mesenchymal to amoeboid transition (see also [Ruprecht et al., \[2015\]](#) in this issue of *Cell* for more details on the model). The model treats the actin cortex as an active gel of density $\rho(x)$ and linear extension L , which undergoes turnover: the depolymerization rate is denoted k_d and the polymerization rate $\rho_0 k_d$ (here ρ_0 can be interpreted as the density of a homogeneous cortex at steady state). Mass conservation can then be written

$$\partial_t \rho + \partial_x(\rho v) = -k_d(\rho - \rho_0),$$

where v denotes the velocity of cortical flow in a fixed reference frame (the reference state is here an immobile cell). Force balance can be written

$$\partial_x(\sigma^a - \Pi) = \xi v$$

where the active stress $\sigma^a = \zeta \rho^2/2$ accounts for actomyosin contractility ($\zeta > 0$ is here a phenomenological parameter modeling contractility), ξ is the friction coefficient that is controlled by adhesion strength, and $\Pi = (\beta/3)\rho^3 - \gamma \partial_x^2 \rho$, where $\beta > 0$, $\gamma > 0$ is the osmotic pressure. This defines the dynamics of the problem. Looking for solutions of the form $\rho(x, t) - \rho_0 \sim e^{\lambda_n t} \cos(n\pi x/L)$, the linearized dynamics yields the dispersion relation

$$\lambda_n = -k_d + \frac{1}{\xi} \left(\frac{n\pi}{L} \right)^2 \left(\zeta \rho_0^2 - \beta \rho^3 - \left(\frac{n\pi}{L} \right)^2 \gamma \right).$$

This equation reveals that the balance of contractility and friction drives the linear instability of the gel, which is obtained when $\lambda_n > 0$; the mixing effect of filament depolymerization suppresses long wavelength modes, and the smoothing term proportional to γ cuts off short wavelength modes. At sufficiently high contractility ζ , $\lambda_1 > 0$ and an initially homogenous static cortex becomes unstable toward a polarized state with increased actin density at the rear and long-lived actin retrograde flows sustained by contractility and turnover, as depicted in [Figure 6H](#). As a result of friction between cortex and the confining surfaces (mediated by transmembrane proteins) momentum is transferred and cell motility induced. The condition $\lambda_1 > 0$ defines the region of amoeboid auto-polarized mode A2 in the phase diagram of [Figure 7C](#).

SUPPLEMENTAL REFERENCES

- Betz, T., Koch, D., Lim, D., and Käs, J.A. (2009). Stochastic actin polymerization and steady retrograde flow determine growth cone advancement. *Biophys. J.* 96, 5130–5138.
- Dickinson, R.B., and Tranquillo, R.T. (1993). Optimal estimation of cell movement indices from the statistical analysis of cell tracking data. *AIChE J.* 39, 1995–2010.
- Gail, M.H., and Boone, C.W. (1970). The locomotion of mouse fibroblasts in tissue culture. *Biophys. J.* 10, 980–993.
- Lancaster, O.M., Le Berre, M., Dimitracopoulos, A., Bonazzi, D., Zlotek-Zlotkiewicz, E., Picone, R., Duke, T., Piel, M., and Baum, B. (2013). Mitotic rounding alters cell geometry to ensure efficient bipolar spindle formation. *Dev. Cell* 25, 270–283.
- Le Berre, M., Zlotek-Zlotkiewicz, E., Bonazzi, D., Lautenschlaeger, F., and Piel, M. (2014). Methods for two-dimensional cell confinement. *Methods Cell Biol.* 121, 213–229.
- Poser, I., Sarov, M., Hutchins, J.R.A., Hériché, J.-K., Toyoda, Y., Pozniakovsky, A., Weigl, D., Nitzsche, A., Hegemann, B., Bird, A.W., et al. (2008). BAC TransgeneOmics: a high-throughput method for exploration of protein function in mammals. *Nat. Methods* 5, 409–415.
- Riedl, J., Crevenna, A.H., Kessenbrock, K., Yu, J.H., Neukirchen, D., Bista, M., Bradke, F., Jenne, D., Holak, T.A., Werb, Z., et al. (2008). Lifeact: a versatile marker to visualize F-actin. *Nat. Methods* 5, 605–607.
- Selmeczi, D., Mosler, S., Hagedorn, P.H., Larsen, N.B., and Flyvbjerg, H. (2005). Cell motility as persistent random motion: theories from experiments. *Biophys. J.* 89, 912–931.
- Stokes, C.L., Lauffenburger, D.A., and Williams, S.K. (1991). Migration of individual microvessel endothelial cells: stochastic model and parameter measurement. *J. Cell Sci.* 99, 419–430.

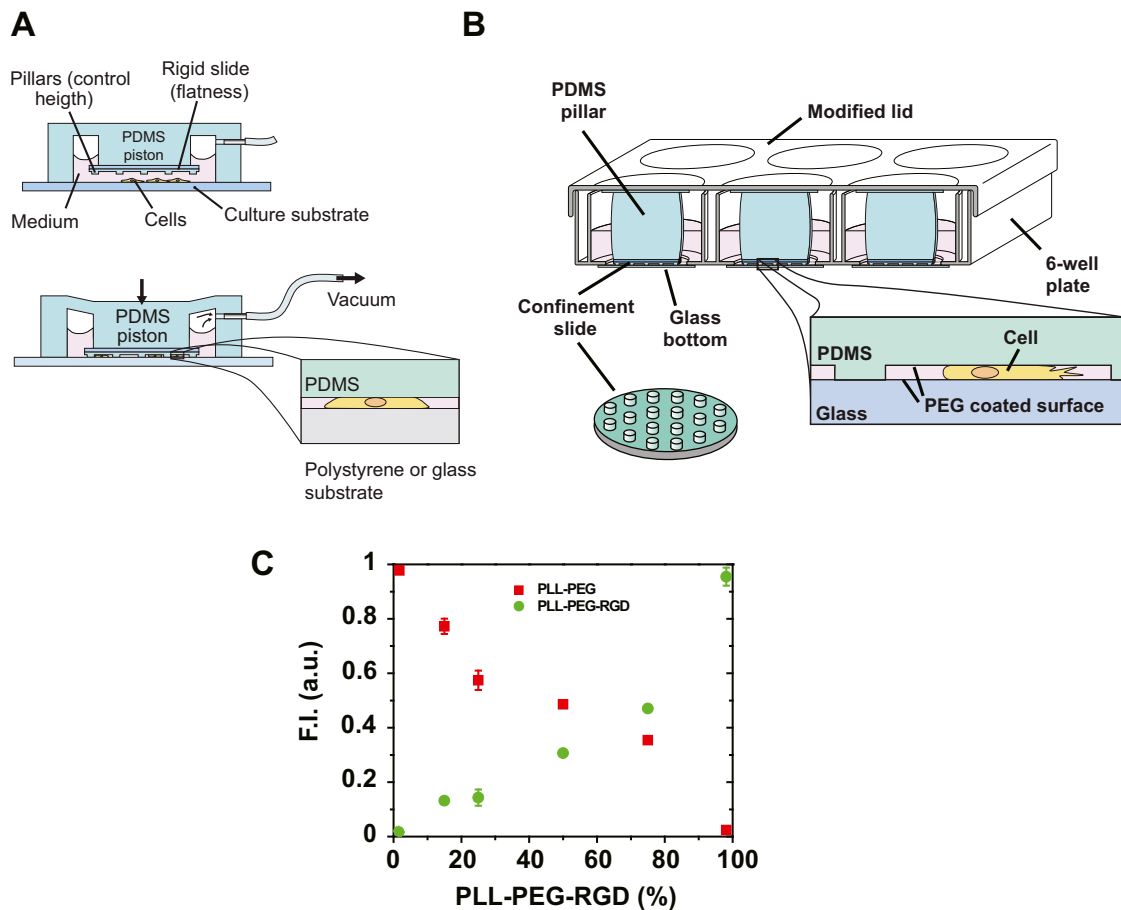


Figure S1. Set-Up of the Devices, Related to Figure 1

(A) Schematic of the cell confinement apparatus (modified from [Le Berre et al., 2012](#)).

(B) Schematic of the modified 6-well plate for cell confinement (modified from [Le Berre et al., 2014](#)).

(C) Characterization of pLL-PEG-RGD-Alex-488 density adsorbed on the surface by fluorescence as a function of the percentage of pLL-PEG-RGD-Alex-488 in both pLL-PEG-Alex-594 and pLL-PEG-RGD-Alex-488 solution used for coating. Fluorescence intensity was quantified by integrating the signal over a field of view of a microscope equipped with the quantitative cooled CCD camera coolsnap HQ (Photometrics).

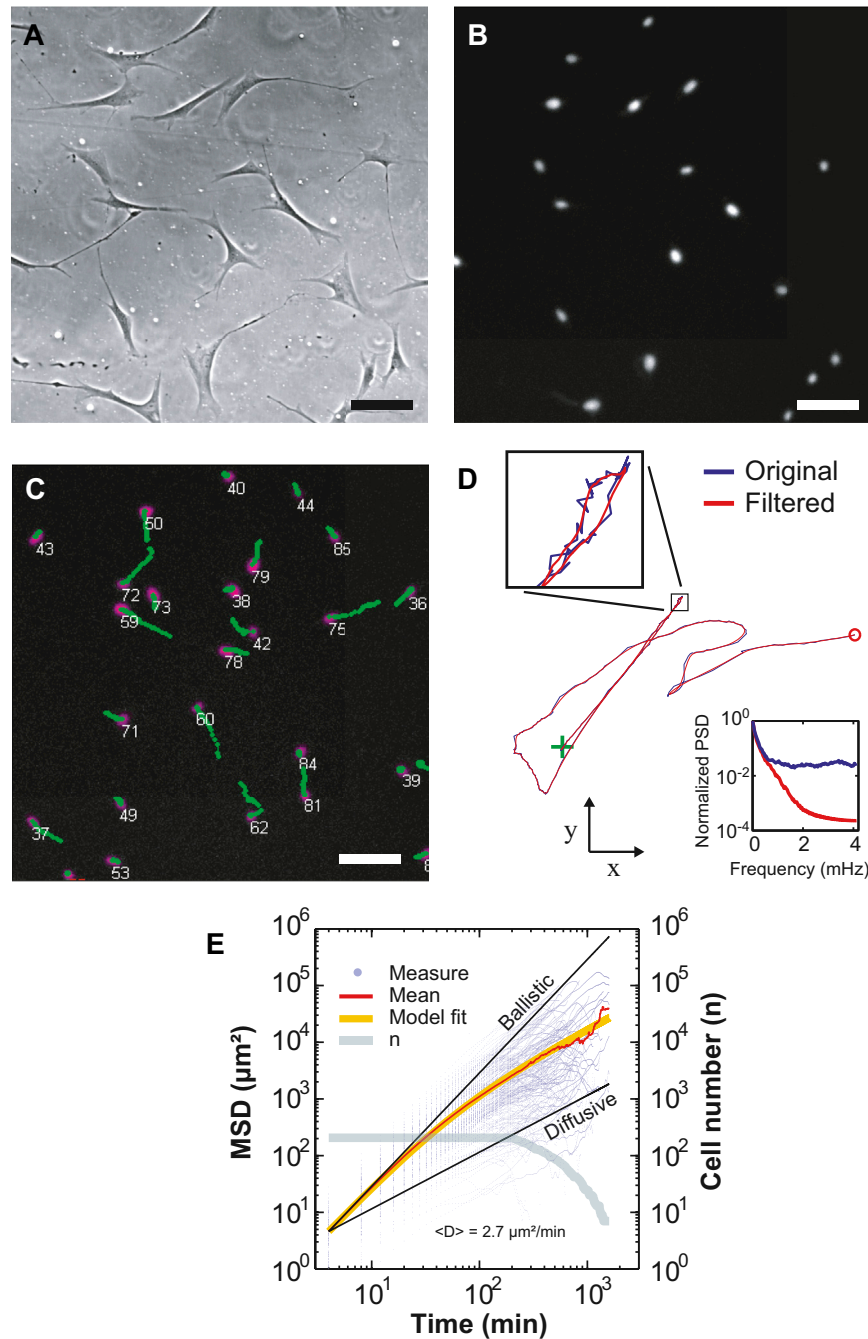


Figure S2. Cell Trajectories Analysis, Related to Figure 2 and Movie S1

(A) Typical phase contrast image extracted from a time-lapse recording of NHDF cells.

(B) Corresponding fluorescence image of the nuclei stained with HOECHST.

(C) Migration trajectories overlaid on the image of nuclei at time 0.

(D) Typical non filtered (blue) and filtered (red) trajectory of a cell nucleus. Green cross corresponds to the initial position and red circle to the final one. Insert shows the normalized power spectral density (PSD) of cell trajectories of the full experiment before and after filtering. Arrows are $20 \mu\text{m}$.

(E) Mean square displacement (MSD) of individual cells calculated with the overlapping intervals method (blue), mean for all cells (red), fitted with the Furth model (yellow) and corresponding number of tracks used for the calculation of the mean (gray). Black lines are visual guides showing the slope of the limit cases of ballistic and diffusive modes of migration. (A-D) corresponds to a non-confined case on a 100% pLL-PEG-RGD surface and (E) to a non-confined case on 15% pLL-PEG-RGD surface. All scale bars are $100 \mu\text{m}$.

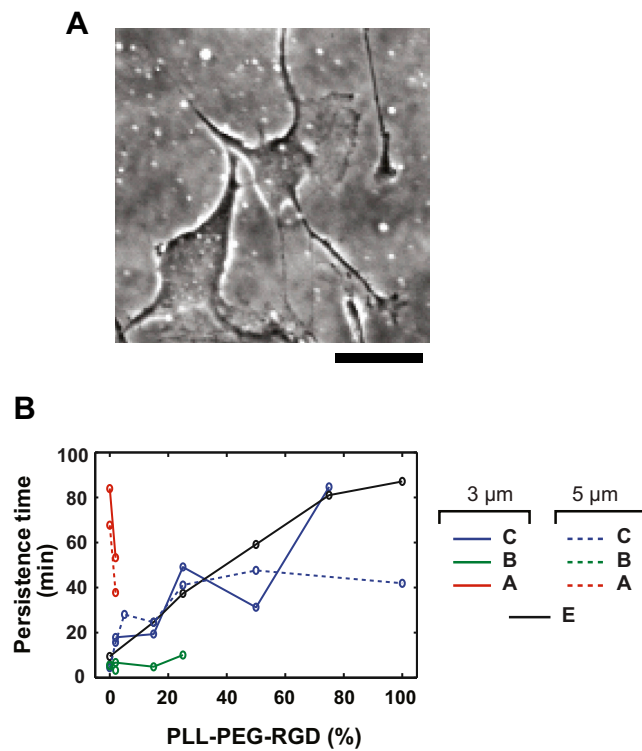


Figure S3. NHDF under Confinement, Related to Figure 3

(A) NHDF cell morphology when plated on 100% pLL-PEG-RGD and confined with a 3 μm gap. Scale bar is 50 μm .

(B) Persistence time measured on cell trajectories analyzed in Figure 3E. Note on blebbing under confinement: $57.8\% \pm 4.3\%$ of cells blebbing at 0% RGD 5 μm confinement and $27\% \pm 3.7\%$ of cells blebbing at 75% RGD 3 μm confinement, whereas no cell showed blebs without confinement or with weak confinement (5 μm) and strong adhesion.

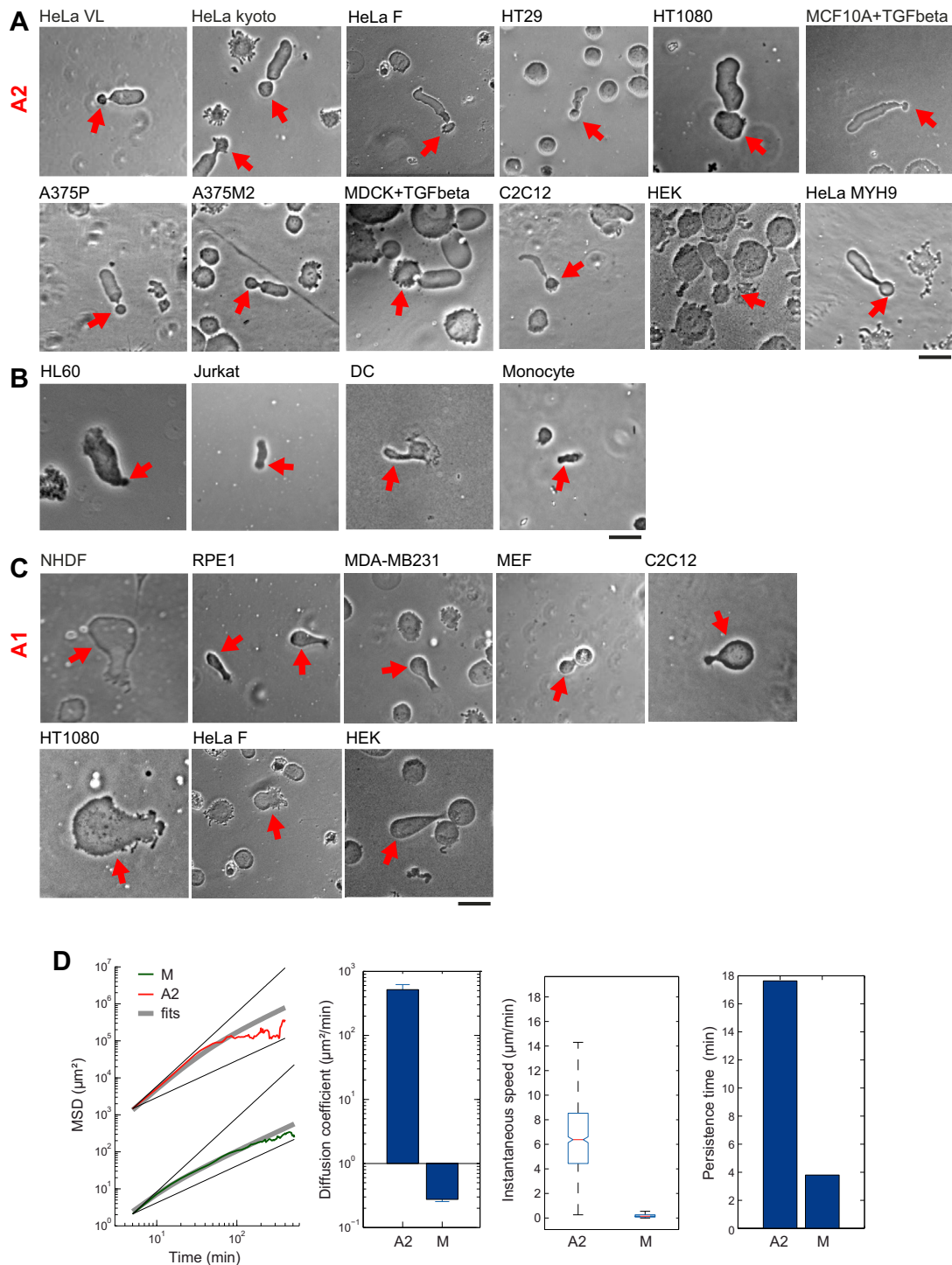


Figure S4. Phenotypes for Different Cell Lines under 3 μm Confinement, Related to Figure 4

(A–C) Phase contrast image showing representative cells of the A2 phenotype (A), A2-like phenotype of immune cells (B) and A1 phenotype (C), for the different cell types tested. For all images, confinement is 3 μm and surfaces are treated with PEG. Bars are 50 μm . Red arrows indicate the back of cells of interest.

(D) Comparison of migration parameters for HeLa VL in their mesenchymal migration mode (M) on a fibronectin-coated surface and in A2 amoeboid mode when confined at 3 μm height on a PEG-coated surface. From left to right: Mean Square Displacement (MSD) and Furth model fits; Diffusion coefficient, Instantaneous speed and Persistence.

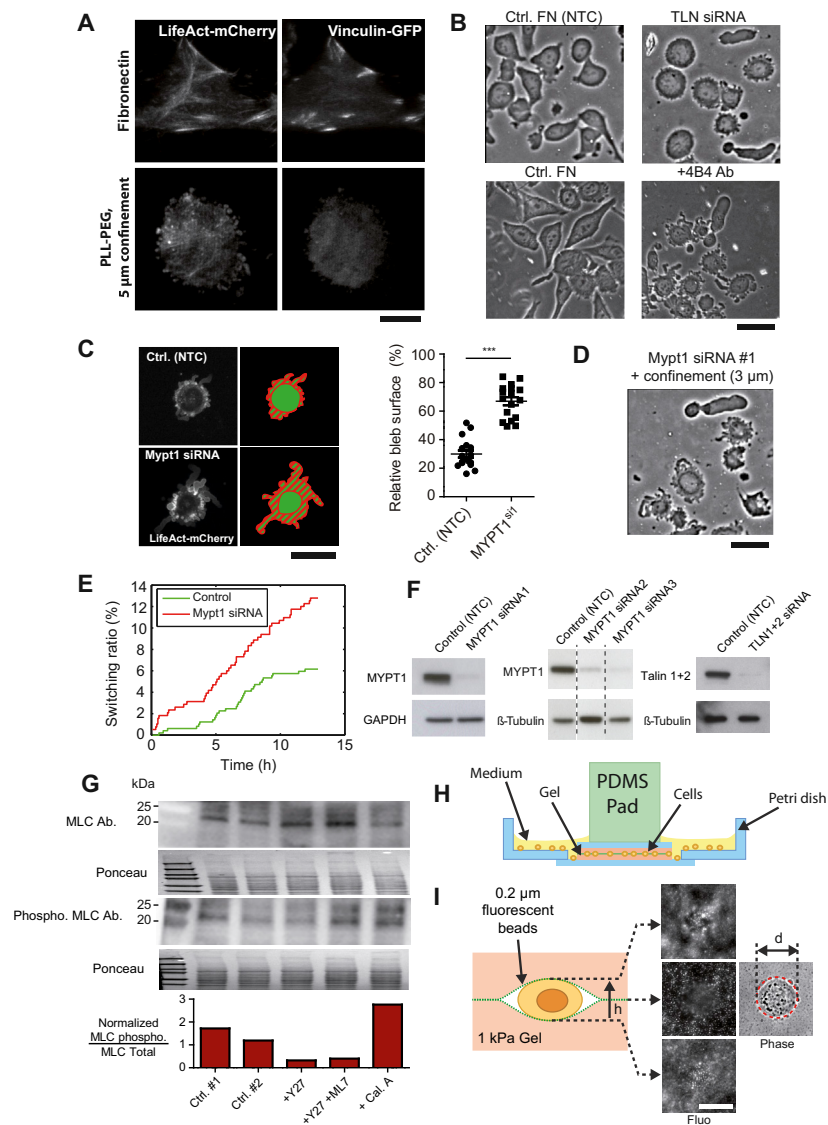


Figure S5. Control Data for siRNA Treatments, Related to Figure 5

(A) TIRF microscopy images of HeLa VL cells expressing both LifeAct-mCherry and vinculin-GFP (left, right), under two conditions: on fibronectin-coated adhesive surface without confinement (top) and after 5h under mild confinement (5 μ m) pushing the cell against a non-adhesive PEG surface (bottom). Scale bar is 10 μ m.

(B) Characteristic images of cells confined on an adhesive surface (fibronectin coated) treated with a non-targeting control (NTC) siRNA, with a siRNA targeting TLN1 and TLN2 (top panel), without treatment or with 4B4 antibody against β 1 integrins (bottom panel). As expected, cells detached from the surface when they were not confined, indicating that the siRNA was effective in preventing the formation of focal adhesions. Scale bar is 50 μ m.

(C) MYPT1 siRNA treated cells (bottom left image) exhibited more blebbing activity than cells treated with an NTC siRNA (upper left image). Right graph: measure of the surface of blebs (dashed red area on the scheme) relative to the total surface (green on the scheme) ($n = 17$ cells for each condition). Scale bar is 20 μ m.

(D) Characteristic images of cells confined on a non-adhesive surface (pLL-PEG) treated with a siRNA targeting MYPT1. Scale bar is 50 μ m.

(E) Ratio of cells having switched toward an A2 mode of migration before a certain time.

(F) Western blot control of TLN and MYPT1 siRNAs 48 hr after treatment.

(G) Quantification of Phosphorylated MLC ratio (bottom). The ratio is calculated by dividing the normalized amount of phosphorylated MLC (Phospho. MLC Ab) by the normalized amount of total MLC (MLC Ab). Quantifications are normalized by the total amount of protein in the lane measured with a Ponceau S staining (Ponceau Images are compressed vertically for the sake of visibility).

(H and I) Schematic of the contractility index measurement method. Cells were confined between two thin polyacrylamide gels of 1kPa stiffness containing 200 nm fluorescent beads on their surface. The bottom gel was polymerized on a 35 mm thin glass bottom petri dish and the top gel was pressed on the first gel with a PDMS weight. (H) The height h of the cell is calculated measuring the distance between planes where beads on the top and under the bottom of the cells are in focus (Fluo images on the figure). The diameter d of the cell is measured on the phase image. (I) The contractility index, defined as h/d , corresponded to the ability of the cell to resist the gel pressure. Scale bar is 20 μ m.

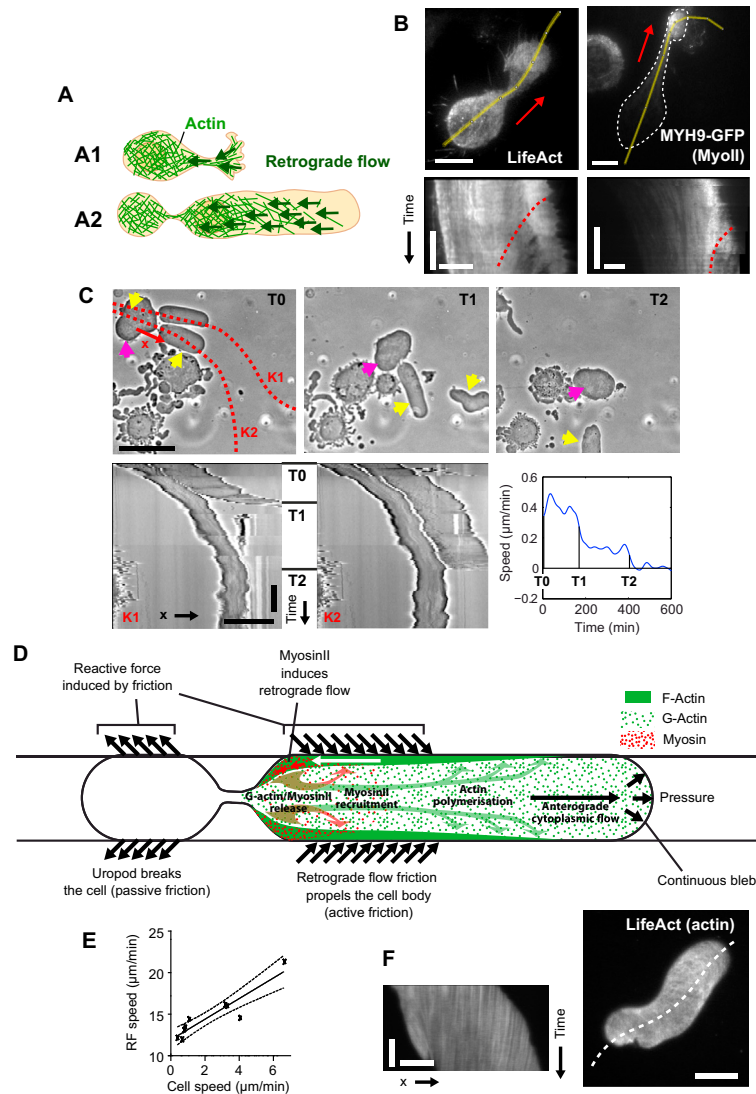


Figure S6. Retrograde Flow Analysis, Related to Figure 6 and Movie S8

(A) Scheme illustrating the localization of the propulsive retrograde flow in A1 and A2 modes of migration.

(B) Representative TIRF microscopy images of LifeAct-mCherry on HeLa VL (left), and of MYH9-GFP expressing HeLa Kyoto cells (right) on A1 moving cells. Cells were confined under $3\ \mu\text{m}$ on a non-adhesive PEG surface. Bottom images correspond to kymographs showing retrograde flow in the protrusive front (the dashed red line is a visual guide showing the retrograde flow). White dashed line shows the cell outline on the myosin II image, yellow lines were used to generate kymographs and red arrows show the direction of cell motion. Horizontal bars are $10\ \mu\text{m}$ and vertical bars are 2 min.

(C) Migration behavior of a cell losing two fronts successively. The cell back (pink arrow) is tracked by the cell fronts (yellow arrows). Two kymographs (bottom images) individually tracking cell fronts over the paths K1 and K2: the cell back speed was highest with two leading blebs, intermediate when only one bleb was left (after T1), and stopped when both blebs were detached (after T2). The speed of the cell back, measured on the right kymograph is shown on the bottom right graph. Horizontal bars are $50\ \mu\text{m}$ and vertical bar is 100 min.

(D) Schematic summarizing the mechanisms underlying the motility of A2 cells. In A2 cells, we observed that the cell body, where the retrograde flow was observed, was dragging the uropod, where actin was static (in the reference frame of the cell). Indeed, in cases in which the neck between the cell front and the uropod ruptured, which often occurred, the cell moved faster and the uropod stopped. This observation was even more striking in some rare cells displaying two large stable blebs (C). In such cells, the speed of the uropod depended on the number of pulling blebs (C). From these observations, we hypothesized that two opposite forces were acting on the cell body (D). The coupling of the actin retrograde flow to the substrate (active friction) was responsible for the cell's motion. At the same time, the uropod was being dragged, producing passive friction and acting as a break, slowing the cell's motion.

(E) Correlation between the cell speed and the retrograde flow speed (in the reference frame of the cell).

(F) TIRF microscopy images of a HeLa VL cell expressing LifeAct-mCherry in the A2 mode of migration after loss of its uropod (right image, $3\ \mu\text{m}$ confinement on a non-adhesive PEG surface). Left image is a kymograph showing the retrograde flow in the fragment. Note the vertical lines showing that actin almost does not move relative to the substrate, suggesting that there is no slippage when the passive uropod is not being dragged by the cell. The white dashed line was used to generate the kymograph. Horizontal bars are $10\ \mu\text{m}$ and vertical bar is 2 min.